ACTIVATION OF CdTe SOLAR CELLS USING MOLECULAR CHLORINE

by

Jason Trevithick

A thesis submitted to the Faculty and Board of Trustees of the Colorado School of Mines in partial fulfillment of the requirements for the degree of Master of Science (Chemical Engineering).

Golden, Colorado

Date _____

Signed: _____

Jason R. Trevithick

Signed: _____

Dr. Colin A. Wolden
Thesis Advisor

Golden, Colorado

Signed: _____

Signed: _____

Dr. David W.M. Marr
Professor and Head
Chemical and Biological Engineering Department

ABSTRACT

Cadmium telluride-based photovoltaics are presently the leading commercialized thin film solar cell technology. A critical step during device fabrication is exposure of the as-deposited CdTe absorber to $CdCl_2$ vapor at ~400 ºC for 10 – 30 min. This step is critical for obtaining high power conversion efficiencies and has been correlated with recrystallization and grain growth, passivation of grain boundaries, and heterojunction interdiffusion. This activation step is difficult to control and capex intensive. In addition, the use of $CdCl_2$ presents a significant environmental concern due to its high solubility in water. In this thesis we explored molecular chlorine (Cl_2) as an alternative to $CdCl_2$ for activation of CdTe solar cells. This activation treatment could potentially serve as a direct replacement for $CdCl_2$ processing in commercial module manufacturing.

Molecular Cl_2 diluted in N_2/O_2 mixtures was exposed to as-deposited FTO/CdS/CdTe stacks in a custom-built quartz tube furnace, enabling independent control of Cl_2/Ar flowrate (1 – 5 sccm), temperature (375 – 420 ºC), oxygen concentration (0 – 25 %), and treatment time (0 – 10 min). The (111) texture coefficient was tracked during experiments to measure extents of recrystallization as parameters were explored, followed by correlations with device performance. Within the parameters explored it was found that a threshold temperature of T ≥ 400 ºC was required for recrystallization of the films. This coincides with the typical optimum temperature used for $CdCl_2$ activation. In stark contrast to $CdCl_2$ activation, very short treatment times (~1 min) and no oxygen ambient were needed for optimal device performance. In addition, the Cl_2 process delivered significantly improved uniformity and run to run reproducibility relative to conventional $CdCl_2$ activation. The Cl_2 process also displayed a much larger

process window with respect to temperature and eliminated delamination. A final optimization of 1.5 sccm of 3% Cl_2/Ar, T = 415 ºC, 800 sccm N_2, and 2 min resulted in an 11.6% efficient device with an open circuit voltage > 800 mV. This value surpasses the best reports in the literature (9-10 %) and exceeds that of many alternative activation agents (HCl, NaCl, etc.).

Best device performance was less than the 14.5% baseline efficiency achieved with standard $CdCl_2$ treatment. Device characterization revealed losses in both V_{oc} (~50 mV) and J_{sc} (2-3 mA/cm^2). Quantum efficiency showed that collection in the bulk CdTe region was 10% lower than standard $CdCl_2$ activation, suggesting defect-based bulk recombination. Transmission electron microscopy and elemental mapping revealed that grain coalescence was incomplete under Cl_2 activation, leaving regions with voids or low density. Both chlorine and oxygen accumulate at these defects, explaining the substandard performance. The optimal chlorine exposure was the lowest that could be reliably delivered, and it is recommended that further studies reduce the Cl_2 concentration by an order of magnitude or more. In addition, longer times may be required to improve grain coalescence and extend interdiffusion at the heterojunction. The source of oxygen impurities is unclear and requires further investigation. Nevertheless these initial studies are quite promising and a pathway is provided to further improve Cl_2 activation and enable its use as a cost-effective alternative to conventional $CdCl_2$.

TABLE OF CONTENTS

LIST OF FIGURES

LIST OF TABLES

ACKNOWLEDGEMENTS

I am most grateful to my advisor, Colin Wolden, for teaching me the basic skills required for performing research and having endless patience with me throughout the entire process of this degree. I would also like to thank the two remaining members of my thesis committee, Tim Ohno and Sumit Agarwal, for helping me analyze and shape my thesis into a quality body of scientific and critical writing. Jiaojiao Li and Joe Beach also deserve credit for assisting me in learning the CdTe solar cell fabrication process at CSM in addition to showing me the basics in maintaining and setting up research equipment. Deanna Jacobs and Anne Messerli in the Department of Chemical and Biological Engineering were the ones that enabled solutions to all of the practical issues that are associated with earning a graduate degree. My mother and father also deserve credit for always being there for me and supporting my path to education. I gratefully acknowledge the Bay Area Photovoltaic Consortium for their support of this work performed under U.S. Department of Energy Award number DE-EE0004946.

CHAPTER 1

INTRODUCTION

This chapter serves as an overall introduction to CdTe solar cells, beginning with an explanation of why photovoltaic energy is needed, followed by a review of alternative solar cell technologies and solar cell device physics.

1.1 The Terawatt Challenge

Carbon emissions are becoming a unifying topic in the many fields of modern science and engineering. The driving force behind this trend is the approximately linear relationship between atmospheric CO_2 concentrations and global warming, as seen in Figure 1.1, in combination with the large fraction of world energy production presently derived from fossil fuels. The effects of climate change from fossil fuels such as more frequent droughts, erratic weather patterns, and decreased water quality, result in significant economic and quality of life losses, particularly in developing countries where these impacts are more far reaching. In addition to climate change, another disadvantage is that fossil fuels are considered to be non-renewable, existing as finite reserves that must be identified and subsequently developed until a non-sustaining point of diminishing returns is reached. In 2015 the Organization for Economic Co-operation and Development with affiliated International Energy Agency released a report indicating the 2013 world consumption of energy was 9301 million tonnes of oil equivalent (Mtoe)[1], corresponding to an average power usage rate of 12 terawatts (TW). Of the consumed 12 TW for that , 3 TW[2] was due to the United States, and the world energy demand is projected to be 30 TW by mid-century. As a consequence of

these large demands, about 20 TW will need to be generated from non-carbon emitting sources in 2050 to begin the process of stabilizing CO_2 in the atmosphere from releases that have occurred since the dawn of industrialization.

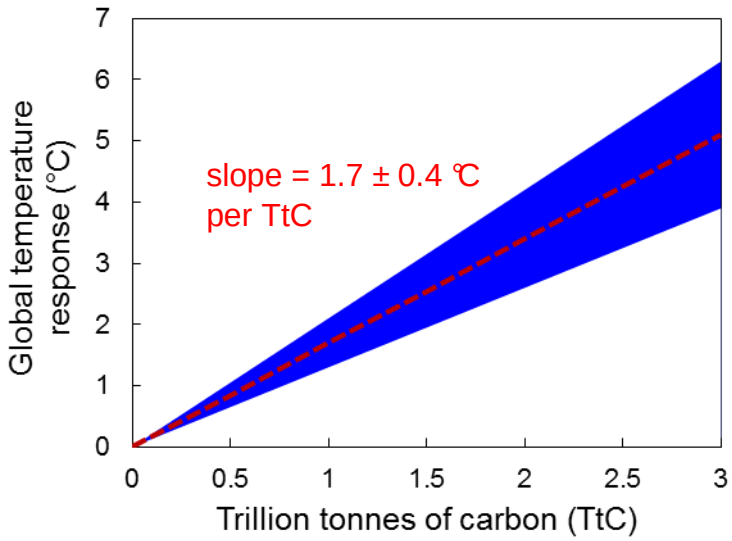

Figure 1.1 Approximately linear relationship between global warming and atmospheric CO_2. The blue region represents one standard deviation of uncertainty. Adapted from [3].

This paradigm shift in electricity production is known as the “Terawatt Challenge”[4] and will likely be realized by photovoltaic solar energy due to its immense energy potential. This is because the combined global resources from hydroelectric, geothermal, wind, and biomass is estimated to be 10 TW, which is comparatively much less than the 50 – 1500 TW potential for solar[5]. Although biomass, hydroelectric, and wind have much lower energy reservoirs, these technologies are also considered Terawatt candidates as evidenced by their majority makeup of the current renewable energy market. Out of all of the renewables, the solar energy sector showed the greatest growth with a 54 % change in installed capacity and 33.6 TWh total energy

generation in 2014 for the US[6]. Terawatt scale viability from PV is further demonstrated by considering that the average cost of grid electricity steadily increased from 8.14 ¢/kW·h[7] in 2005 to 10.4 ¢/kW·h[7] in 2014 while the median installed price for utility scale PV projects decreased from 68 ¢/kW·h in 2007-2009 (reported as \$6/W_{AC}[8]) to 34 ¢/kW·h in 2014 (\$3/W_{AC}[8]). Once conventional grid costs become equal to installed module costs, known as grid parity, it is assumed that widespread installations of PV will occur, becoming self-sustaining without the need of government subsidies. Continual innovations in PV technologies with recent federal regulations such as the EPA's Clean Power Plan and Mercury and Air Toxics Standards Rule will ensure that these trends in energy cost will continue, eventually resulting in widespread grid parity. For certain regions of the US, grid parity has in fact already been reached. Although the PV industry is relatively new, there is tremendous capacity for usag non-carbon emitting source of TW scale energy.

1.2 Photovoltaic Basics

Solar cells are composed of semiconductor materials that are contacted with metals in order to produce DC power from illumination by the sun. These same materials and the science and engineering of their chemical, electrical, and structural properties are also used for the fabrication of circuit devices such as transistors, diodes, and capacitors. Semiconductors can be elemental such as Si (group V material), binary compounds as is the case for CdTe (II-VI) and GaAs (III-V), or more complex alloys such as $CuIn_xGa_{(1-x)}Se_2$ (I-III-VI_2). All solid state materials (insulators, semiconductors, and metals) consist of many overlapping atomic orbitals from adjacent atoms. As a

result of this the discrete energy levels of neighboring atoms become finely spaced forming continuous band of energies where electrons become delocalized to various degrees allowing formation of ionic, covalent, metallic, or Van der Waals atomic bonds [9]. For a semiconductor or insulator, the outermost occupied band is the valence band with it being completely filled at 0 K. Above this is the conduction band and is completely unoccupied at 0 K.

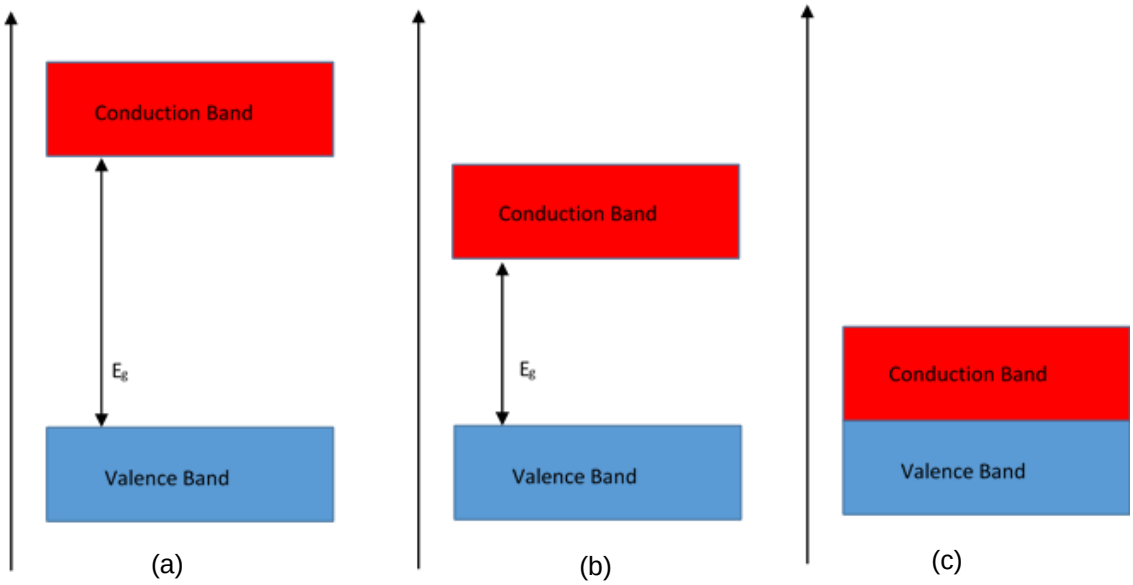

Figure 1.2 Band diagrams of an (a) insulator, (b) semiconductor, and (c) metal

At temperatures greater than 0 K electrons can be thermally excited to the conduction band, producing mobile charge carriers and conductivity. Similarly an absence of an electron, known as a hole, in the valence band is a charge carrier and contributes toward electrical conduction. The energy between the valence band maximum and conduction band is the band gap (E_g) and as shown above in Figure 1.2 is very large for

insulators (>9 eV), intermediate for semiconductors (1-3 eV), and nonexistent for metals.

Although the bandgap of semiconductors is much less than insulators, at 300 K the amount of thermal energy is only enough to excite very few electrons to the conduction band giving a small intrinsic carrier concentration, for the case of Si (E_g = 1.1

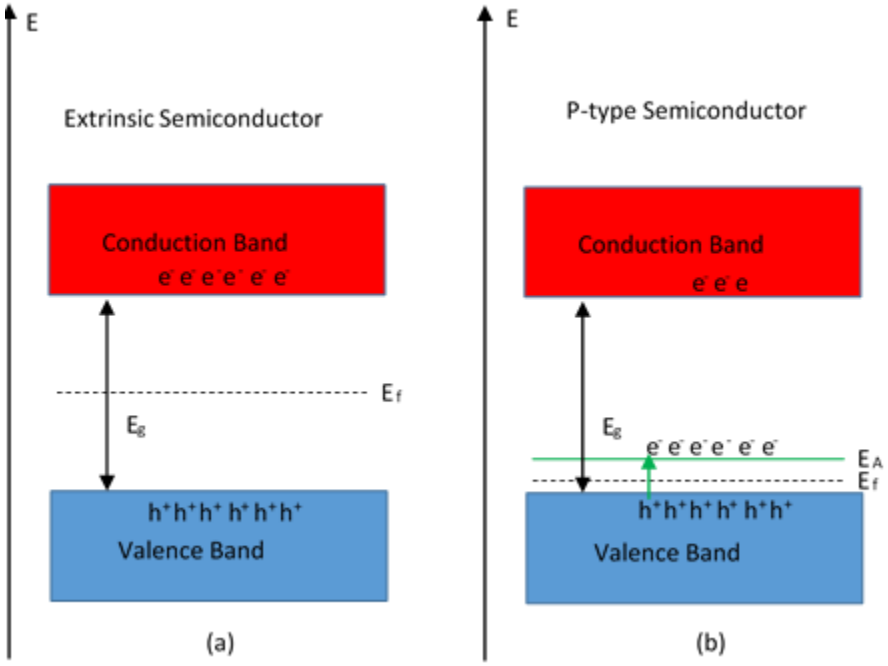

Figure 1.3 Band diagram of an (a) extrinsic and (b) p-type semiconductor.

eV and kT = 0.03 eV), 10^{-10} cm^{-3}[9]. As a result of this the fermi level (E_f), being defined as the energy at which a 50 % chance of electron occupation occurs, is equal to approximately $E_g/2$ for intrinsic semiconductors. The fermi level and therefore conductivity (p-type or n-type) of a semiconductor can be modified by the addition of impurity dopants or defect energy states within the bandgap. Band diagrams of an intrinsic and p-type semiconductor are shown in Figure 1.3. Acceptor energy states (E_A) are located near the valence band as seen in Figure 1.3(b) and are able to accept

electrons, making holes the majority carrier and shifts the fermi level between E_A and the valence band. If the energy state is near the conduction band (donor - E_D), it can be easily thermally ionized to donate extra electrons to the band and electrons become the majority charge carrier in the semiconductor (n-type conductivity).

A solar cell is essentially a p-n diode, consisting of a p-type semiconductor brought into metallurgical contact with an n-type region, and the bandgap of the semiconductor is on the order of the solar spectrum, thus allowing for charge carriers to be generated. If the p-n junction is formed from a single semiconductor (e.g. p-type Si and n-type Si) it is a homojunction solar cell and is called a heterojunction if it is formed with two different materials (e.g. CdTe and CdS). When the n- and p-type regions are contacted, majority carrier electrons diffuse from the n-type to p-type and holes correspondingly diffuse in the opposite direction[9]. As electrons and holes diffuse, fixed positively charged donor atoms on the n-type side and fixed negatively charged

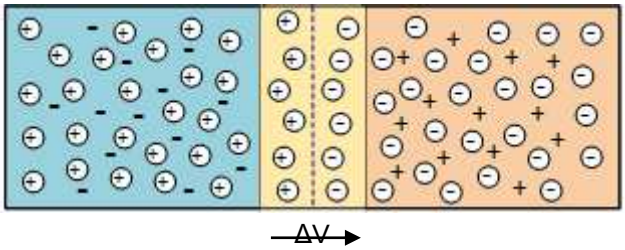

Figure 1.4 Depletion region of a p-n junction[10].

acceptor atoms on the p-type side of the interface set up a net electric field that opposes the direction of diffusion, seen as the yellow area in Figure 1.4. This diffusion occurs until a necessary width depleted of majority carriers at the p-n interface has been reached allowing for the electric field to balance the diffusion force[9].

It is this built in potential drop at the p-n junction that allows for photo generated electron-hole pairs to be separated (drift) and transported to electrical contacts to perform work through an external circuit. The electron-hole pairs are first generated by absorption of a photon that has an energy greater than or equal to the band gap. Transport of the pair to the built in potential for separation and contribution towards photocurrent depends on the rate of recombination of the electron-hole pair. The rate of recombination relies relates to minority carrier lifetime and diffusion length, with the mechanism for recombination either being band to band relaxations (radiative), deep level defect traps, or Auger recombination[11]. Once in the depletion region, the alignment of the fermi levels in the n- and p-type regions causes band bending of the

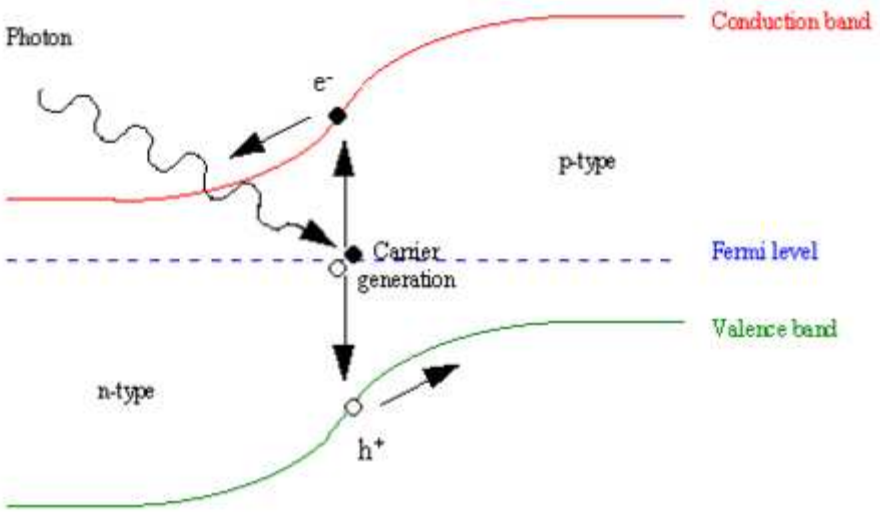

Figure 1.5 Band bending in a p-n junction[12].

conduction and valence bands over the depletion region, as illustrated in Figure 1.5. This band bending allows electrons to travel into the n-type material and for holes to go into the p-type under action of the built in voltage and this generates photocurrent.

The current-voltage characteristics of a solar cell under illumination can be modeled by an equivalent circuit containing a short circuit current source (I_{sc}) in parallel with two diodes that oppose the flow of the current, shown in Figure 1.6, and includes shunt (R_{Sh}) resistor and series (R_S) resistors. Diode 1 in Figure 1.6 constitutes

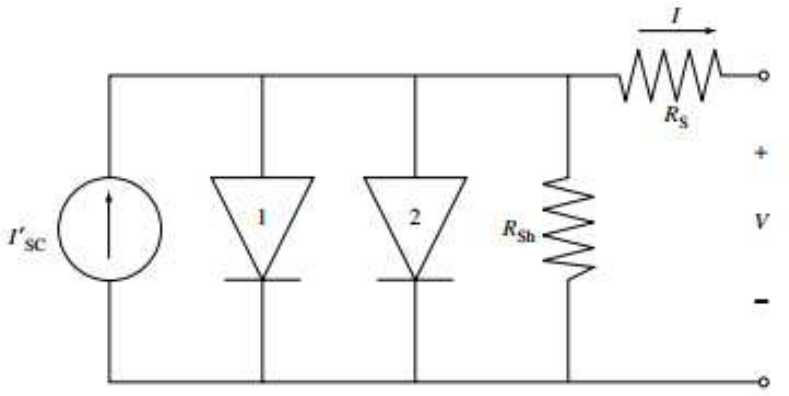

Figure 1.6. Equivalent circuit of a solar cell[13].

recombination in the bulk n- and p-type regions and diode 2 corresponds to recombination currents that occur in the depletion region. R_s is caused by the resistances of the semiconductor thin films and R_{Sh} is due to defects and current leakage across the pn junction. Total current from the solar cell (I) is therefore equal to the short circuit current (I_{sc}) minus current lost in the two opposing diodes and resistors described by Equation 2-1.

$$I = I_{SC} - I_{01}\left(e^{\frac{q(V+IR_S)}{kT}} - 1\right) - I_{02}\left(e^{\frac{q(V+IR_S)}{kT}} - 1\right) - \frac{(V-IR_S)}{R_{Sh}} \qquad (2.1)$$

Where I_{01} and I_{02} represent the dark saturation currents for the two opposing diodes, T is the absolute temperature, V is the voltage across the cell, k is Boltzmann's constant, and q is the elementary charge.

A common plot of current density (J), obtained by dividing the current produced by the cell by the device area, against voltage yields the four central metrics for comparing the performance of different solar cells: open circuit voltage (V_{OC}), short circuit current density (J_{SC}), fill factor (FF), and overall power conversion efficiency (η). A diagram showing typical the typical J-V curve of a solar cell under standard illumination

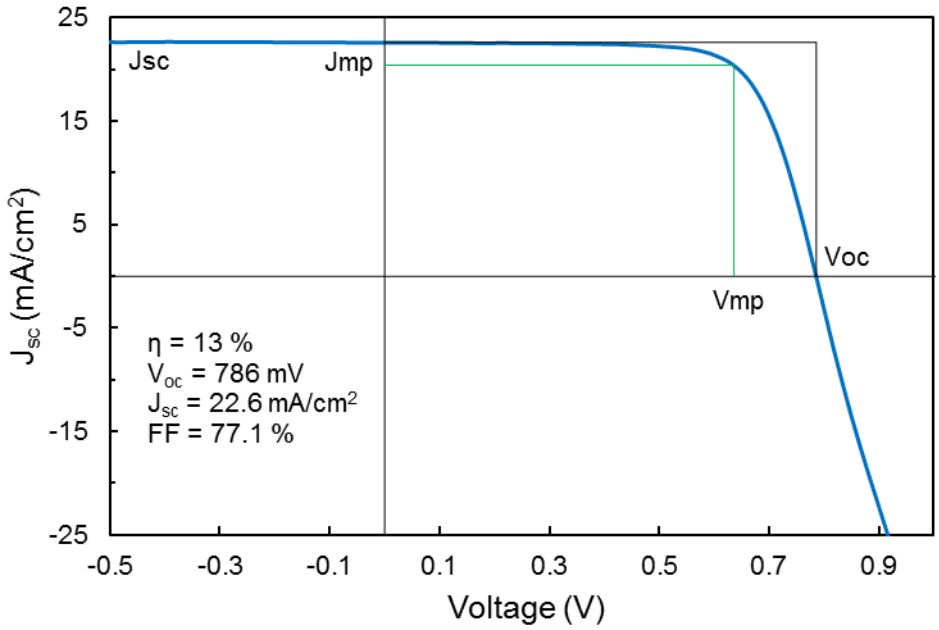

Figure 1.7 J-V characteristics of a 13 % solar cell

conditions (AM 1.5) and characteristics for a 13 % power conversion efficiency are shown in Figure 1.7. When no external load is connected to the terminals solar cell, the resulting voltage is the V_{oc} and corresponds to the x-intercept in the blue J-V curve in Figure 1.7. When the terminals of the cell are shorted, the resulting current is the J_{sc}.

The max power density (P_{mp}) of the device is found when the product JV is maximized and is found at V_{mp} and J_{mp} on the JV curve. The ideality of the device is calculated by:

$$FF = \frac{V_{mp}J_{mp}}{V_{oc}J_{sc}} \qquad (2\text{-}2)$$

This value is graphically seen as the ratio of the green rectangle to black one. The power conversion efficiency is the ultimate metric for comparing several cells because it accounts for all major characteristics of the J-V curve and is calculated by determine the ratio of the device maximum output power to the input device power.

$$\eta = \frac{P_{mp}}{P_{in}}100\% = \frac{FF\ V_{oc}\ J_{sc}}{P_{in}}100\% \qquad (2\text{-}3)$$

1.3 Solar Cell Technologies

Currently the main solar cell technologies that makeup the global solar module production are polycrystalline silicon (poly c-Si), monocrystalline silicon (mono c-Si),

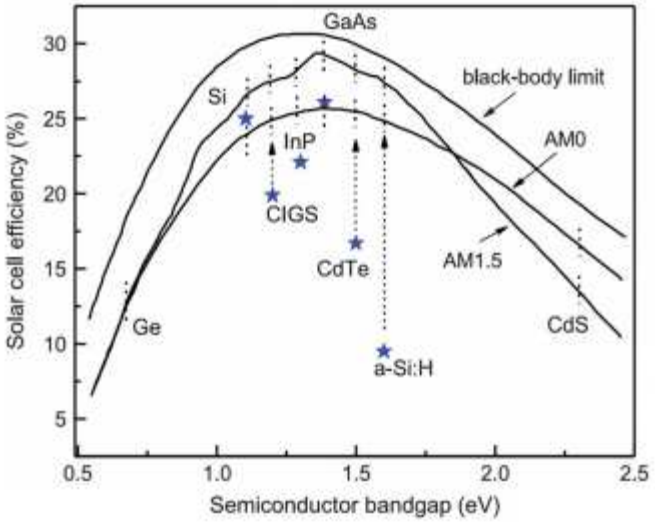

Figure 1.8 Solar cell efficiency as a function bandgap for terrestial illumination[14].

amorphous silicon (a-Si), cadmium telluride (CdTe), and copper indium gallium selenide ($Cu(InGa)Se_2$). The materials denote the absorber material in each solar cell technology and yield highly efficient power conversion efficiencies because of suitable allignment between their bandgaps and the terrestrial AM 1.5 solar spectrum as seen in Figure 1.8. The majority of photovoltaic manufacturing is in poly c-Si and mono c-Si with cumulative module productions for these technologies accounting for 91 % of the 48,961 MW market in 2014[6]. The next largest contributor is CdTe (4 %) followed by a-Si (3%) and CIGS (3%).

Crystalline silicon has dominated in photovoltaics mainly due to the already established Si wafer intrastructure that began in the 1960s, allowing the PV industry to cheaply and quickly adapt much of the already established Si research and technology to create photovoltaic devices. Despite the c-Si majority makeup of the market, a high cost of production for quality crystalline material and a low optical absorption coefficient pose serious drawbacks for the c-Si technologies that will eventually lead to a loosening of its hold on the market. The low optical absorption coefficient is a consequence of its indirect band gap, requiring c-Si cell thicknesses on the order of 100 µm for near complete absorption of the AM 1.5 photons. The charge carriers must exhibit high mobilities in c-Si in order to transport through the material, avoiding defects and recombination sites, to the front and back contacts where power can be extracted. Low defect densities and high mobilities are obtained in Si that is crystalline thus requiring high processing temperatures[13].

The remainder of the major PV technoligies (CdTe, CIGS, a-Si) are direct bandgap materials giving high optical absorption coefficients that enable cells with thicknesses that are two orders of magnitude lower than c-Si for total absorption of AM 1.5 photons . A thinner cell reduces manufacturing costs because less overall material is consumed, and the required defect density is much less than c-Si due to charge carriers traveling shorter distances to the front and back contacts. Out of the thin film PV technologies, CdTe shows great potential to compete with Si as the leading PV material as evidenced by its lower levelized cost of electricity (LCOE) when compared to poly c-Si ($0.11/kWh < $0.14/kWh)[15] and steady increase in champion cell efficiencies (22.1 % in 2016 – First Solar). The CdTe photovoltaic device will remain the central topic for the remainder of the thesis.

1.4 Thin Film CdTe Solar Cells

Cadmium telluride is a II-VI binary compound with a bandgap of 1.45 eV with a thermodynamic potential efficiency of ~30 %. Its high optical absorption coefficient, 5 x 10^5 cm^{-1}, allows for just 2 µm of material to absorb 99 % of the photons with energy greater than E_g = 1.45 eV in the AM 1.5 solar spectrum[13]. At typical processing temperatures (400 – 600 ºC) polycrstalline CdTe gives shallow level cadmium vacancy defects (V_{Cd}) causing p-type conductivity and are suitable to form a p-n heterojunction with n-type CdS (E_g = 2.4 eV)[14]. High efficiency solar cells are deposited in the

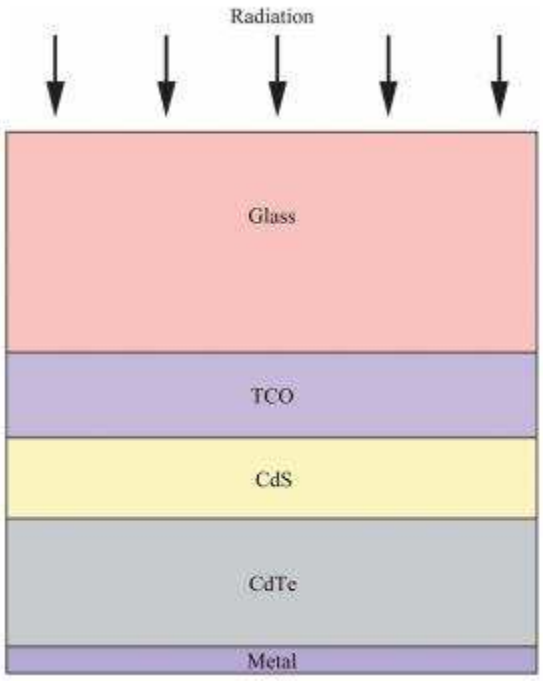

Figure 1.9 CdTe superstrate configuration[14].

superstrate configuration, shown in Figure 1.9, where the front contact/CdS/CdTe/back contact are deposited sequentially onto soda lime glass and light reaches the absorber by entering from the glass substrate.The front contact is a transparent conducting oxide and is either indium tin oxide (ITO), fluorine tin oxide (FTO), or cadmium stannate (CTO) for CdTe/CdS solar cells. TCOs must simultaneously have low sheet resistances and high transmittance in order to allow for photons to reach the absorber and for charge carriers to be extracted. As the thickness of the TCO increases, optical transmission reduces and sheet resistance increases which corresponds to about 150 – 500 nm of thickness for CdTe applications if FTO is used. FTO films are usually deposited onto glass substrates by atmospheric pressure chemical vapor deposition giving an optical bandgap of 3.80 eV, a resistivity less than 10^{-3} Ω·cm, a transmittance of 83 %, and a carrier concentration of 10^{20} cm^{-3}[16]. A highly resistive, transparent

oxide (HRT) layer is sometimes deposited between the TCO and CdS in order to decrease local shunting and increase junction quality by preventing TCO/CdTe junctions. Common materials for the HRT layer include SnO_2[17] and $ZnSnO_x$[18].

The CdS window layer is deposited onto the front contact serving as the n-type partner in the p-n heterojunction and is also a II-VI compound allowing for interdiffusion with CdTe, exhibiting hexagonal wurtzite or cubic zincblende structures (Figure 1.10) depending on the deposition technique and conditions. At higher annealing and deposition temperatures, more of the hexagonal phase of CdS is found. CdS films are commonly deposited by chemical bath deposition (CBD)[21], thermal evaporation[22], metal organic chemical vapor deposition[23], and RF sputtering[24]. A carrier

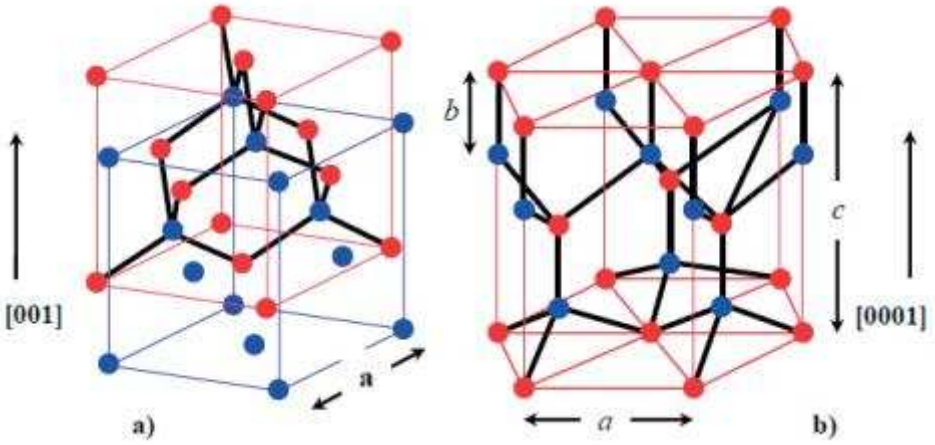

Figure 1.10 Hexagonal wurtzite (a) and (b) cubic zincblende structures[19].

concentration of 10^{16} cm^{-3} is usually obtained in deposited films indicating that the depletion width exists almost entirely in the CdTe layer. Its wide 2.42 eV bandgap ensures that a significant portion of the AM 1.5 photons are not absorbed in the window and can be contribute to photocurrent after being absorbed in the CdTe layer. Some of

the photons with energies equal to or in excess of 2.42 eV can still pass through the window layer by depositing a very thin film of CdS, usually 80 – 200 nm. However, to overcome these losses groups have been developing high bandgap alternative to CdS such as CdS:O, $Cd_xZn_{1-x}S$, and MgZnO.

In accordance with the superstrate architecture, the next thin film to be deposited is the CdTe absorber. A cubic zincblende structure is found for CdTe with a lattice constant of 0.6481 nm, giving a 10 % CdS/CdTe lattice mismatch. Figure 1.11 shows that the vapor pressures of Cd and Te_2 are significantly greater than CdTe, ensuring that only single-phase, stoichiometric depositions are obtained. A congruent sublimation reaction occurs for CdTe that allows the partial pressure of Cd atoms to be twice the

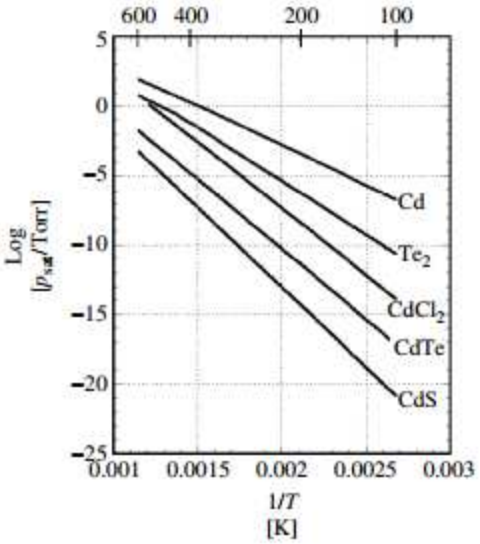

Figure 1.11 Vapor pressure data for absorber and window layer components[13].

partial pressure of Te_2 molecules, giving a vapor phase composition that matches the solid phase stoichiometry[13]. These properties allow for a number of robust commercial manufacturing processes for photovoltaic grade CdTe films, all of which deposit 2-5 µm of polycrystalline material. Some of the common manufacturing

techniques include physical vapor deposition (PVD)[25], closed-space sublimation (CSS)[26], vapor transport deposition (VTD)[27], sputter deposition[28], and electrodeposition[29]. CSS depositions occur by heating a CdTe containing graphite crucible to 650 – 750 ºC at ~1 Torr, causing the mass transfer the of source vapors to become diffusion limited. As a result of this the substrate, independently heat at ~600 ºC, must be brought within several millimeters of the source for 1-5 µm/min deposition rates to occur[13]. The deposition occurs in an inert gas with a small oxygen partial pressure. VTD occurs by convective mass transfer of CdTe onto a substrate from a saturated inert carrier gas as seen in Figure 1.12. Similar to CSS, the substrate temperature is independently controlled from the source in VTD but a carrier gas is introduced at the source which becomes saturated with vapors which then condenses into a film at the substrate when the stream becomes supersaturated. Because convective mass transfer occurs and a moving substrate can be introduce, very large deposition rates occur and this technique is currently the main deposition technique for commercial manufacturing.

After deposition of the absorber, an anneal in a chlorine containing environment, known as the cadmium chloride ($CdCl_2$) treatment or activation, must be performed on the as-deposited CdS/CdTe stack in order for the solar cell to generate reasonable photocurrents and voltages. The performance usually increases by almost an order of magnitude when compared to devices that are not activated. Much of the CdTe research is still focused on this processing step, aiming at an understanding of what conditions lead to material properties that give quality photovoltaic devices[30]. Post-treated devices show intergranular and intragranular recrystallization, grain growth,

interdiffusion at the CdTe/CdS junction, and grain boundary passivation in the absorber layer[31-34]. Higher photocurrents and voltages are obtained because a reduction in recombination centers and defect densities along with increased p-type conductivity, a graded bandgap structure, and removal of lattice mismatch.

Activation treatments are either performed by a solution or vapor-phase processing. Solution treatments begin by dissolving $CdCl_2$ in methanol or deionized water followed by application achieved by dipping the substrate into the solution or spraying the solution on the substrate. The samples are then activated by heating to ~400 ºC for 10 – 30 min in air or a N_2/O_2 mixture. Vapor-phase processing consists of bringing the substrate surface to close proximity of solid $CdCl_2$ and heating the source to ~400 ºC, causing the vapors do diffuse into the substrate. The conditions employed are similar to solution processing. The presence of O_2 in the anneal has been found to be crucial for improvements in fill factor and open-circuit voltage.

After the $CdCl_2$ activation, the final step in fabrication of CdTe solar cells is to deposit ohmic back contacts onto the CdTe layer in order for electrical current to be efficiently extracted. Ohmic contacts are difficult to with CdTe because it is a high-resistivity p-type semiconductor with a high work function (5.9 eV) causing metals, which have considerably lower work functions, to form Schottky barriers. Schottky barriers are undesirable because they are rectifying, allowing current to flow in one direction, and in CdTe the Schottky diode opposes the p-n junction diode, causing limitations in hole transport[35]. Low-resistance ohmic back contacts are formed on CdTe by depositing an interfacial semiconductor layer with properties such as negligible CdTe valence band discontinuity, lower work function, and having an ability for p-type

doping to induce tunneling effects. Common materials used for this method are Cu_xTe ($1 < x < 2$)[36] and ZnTe:Cu [37]. For Cu_xTe depositions, a chemical etch is used to create Te excess on the CdTe surface which then reacts with a deposited Cu film to form the buffer layer. Depositions of ZnTe:Cu films occurs by either sputtering [38] or co-evaporation of Cu and ZnTe onto a chemically etched CdTe surface followed by thermal anneals to optimize the Cu profile. After deposition of the interfacial buffer layer the metal contact is deposited by physical vapor deposition. Gold is often used in laboratories due to its high work function, but numerous other metals have been used including nickel, chromium and titanium.

1.5 CdTe Activation

The focus this thesis was to develop molecular chlorine (Cl_2) as an alternative activation treatment to $CdCl_2$ activation. In this section a brief review of the literature on $CdCl_2$ activation is presented. Challenges of this conventional treatment is discussed along with a review of the results from alternative treatments. Finally, the potential benefits of a gaseous Cl_2 activation are highlighted and the goals of this thesis are enumerated.

Although specific effects due to an activation are primarily a function of the thermochemical history of previously deposited layers, there are common structural, chemical, and optoelectronic properties that are reported when a treatment is properly optimized. Structural and morphological changes usually occur by differences in grain orientation, size, extent of recrystallization, and defect densities to varying intensities after the activation. Intragranular and/or intergranular recrystallization occurs after the

performing the treatment. Intragranular recrystallization almost always occurs, regardless of the exact treatment method and previous deposition methods, causing the orientation of the grains to become more randomized. The extent of intragranular recrystallization is measured with x-ray diffraction. It is generally observed by tracking the change in orientation of the thin film CdTe grains from along the <111> direction (normal to substrate) to becoming randomly distributed. In other words, if the film significantly loses texture in the (111) plane during the $CdCl_2$ activation then recrystallization within each grain must have occurred. Grain coalescence or intergranular recrystallization is observed when the grains increase in mean diameter. Intragranular recrystallization almost always occurs but intergranular does not. Intergranular recrystallization does not occur in CSS or VTD films deposited at high substrate temperatures because the surface energy is pinned before treatment, resulting in large as-deposited grain sizes that do not change significantly in size during activation. Thermal evaporation and sputtering, for example, often employ low temperatures and pressures during deposition which result in small grains in the as-deposited films, indicating that the surface energy has not been pinned yet. After the activation treatment, the thermally evaporated and sputtered films will show grain enlargement.

Recrystallization results in a relaxation of lattice strain, driven by an initial high density of stacking faults with, again, a more drastic change observed for CdTe films grown at low substrate temperatures. Interdiffusion at the CdS/CdTe also occurs by S diffusion into the CdTe layer and Te diffusion into the CdS layer resulting in $CdTe_{1-x}S_x$ and $CdS_{1-y}Te_y$ alloys, respectively. There are both benefits and drawbacks associated

with this process. $CdTe_{1-x}S_x$ formation results in a lower bandgap in the absorber layer due an optical bowing effect in the ternary alloy and causes a beneficial higher long wave photon conversions. The $CdS_{1-y}Te_y$ layer gives a lower bandgap in the window layer due to the optical bowing effect, reducing short wave photon conversions for the device. Another major benefit is that the 10 % lattice mismatch at the CdS/CdTe is significantly reduced and a grading effect in the bandgap can be seen. This results in a decrease in strain and defect densities at the interface. Because the CdS window layer initially very thin compared to the absorber, the interdiffusion can result in complete consumption of the CdS layer causing a reduction in V_{oc}. Shorter $CdCl_2$ have been used on the as-deposited CdS layer in order to prevent subsequent interdiffusion during the CdTe activation [39]. The addition of a separate CdS activation is time consuming so the extent of diffusion is generally controlled and optimized to obtain a maximum device efficiency by varying the CdTe treatment temperature, time, and oxygen partial pressure.

Suitable electronic structures of CdTe for quality heterojunction formation are due to the stabilization of high p-type conductivity, caused by shallow level complexes $(Te_i^{2-}Cl_{Te}^{+})^{-}$ and or $(V_{Cd}^{2-}Cl_{Te}^{+})^{-}$ [40]. Although the enhanced p-type conductivity is important for form a quality heterojunction, the defect complexes are non-uniform throughout the activated CdTe and causes a reduction in V_{oc} [41]. Excess of $CdCl_2$ can also lead to oxychloride precipitates in the CdTe layer and at the junction which causes a detriment to device performance most likely due to insulating effects

Although the $CdCl_2$ treatment is paramount to the CdTe device fabrication sequence, there are numerous drawbacks associated with this process that limit

economic, safety, and processing prospects. Although cadmium is found throughout many layers of the solar cell, these sources do not pose significant environmental risks because these compounds are not water soluble (e.g. CdTe and CdS). $CdCl_2$ is highly soluble in water and is the main source for cadmium emission during device production. Because a high risk of cadmium emission is associated with $CdCl_2$, special infrastructure is required to process and store the material, and this causes the activation treatment to be capex intensive. Treatment times can be as long as 1 hr, significantly adding to the overall manufacturing time for solar cell production, which is highly undesirable because the entire fabrication sequence is inherently a batch process. $CdCl_2$ is a hygroscopic salt that requires periodic removal of the material from annealing furnaces for drying or replacement. Optimization of treatments are quite intricate and easily thrown out of order because the vapor-solid equilibrium couples the concentration and temperature of the $CdCl_2$ molecules. This causes run-to-run control and reproducibility issues in the quality of obtained solar cells from the activation step, which again can be expensive and time consuming.

As a result of the many drawbacks associated with $CdCl_2$ activations, several cadmium-free chlorides, vapors, and gasses have been studied as direct replacements for the activation process. A thermal treatment using a in dry difluorochloromethane (HCF_2Cl) has been investigated in the literature as a gaseous activation treatment[42, 43, 44]. Salavei et al. used atomic force microscopy (AFM) to determine that a slightly higher temperature (420 ºC) was needed for the HCF_2Cl treatment to obtain similar grain sizes (2 µm) and recrystallization when compared to $CdCl_2$ devices treated at

lower temperatures (410 ºC), seen in Figure 1.12. This treatment consisted of 10 mbar of HCF_2Cl in 500 mbar of Ar for 5 - 20 min.

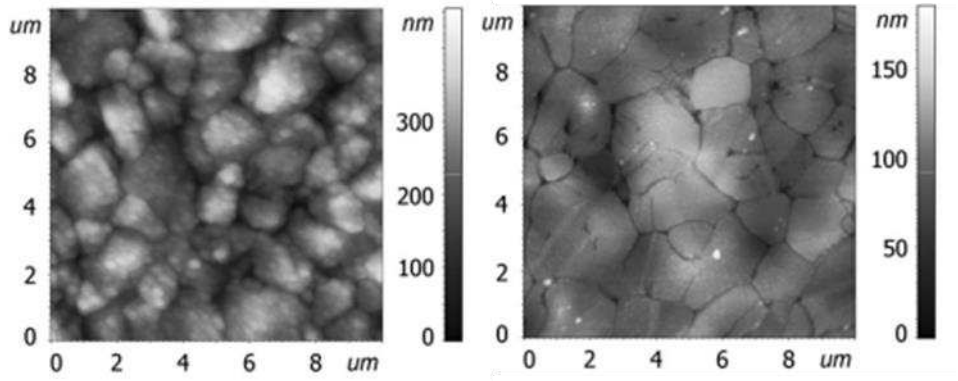

(a) (b)

Figure 1.12 AFM images of CdTe treated with (a) HCF_2Cl at 420 ºC and (b) $CdCl_2$ at 410 ºC showing similar 2 µm diameter grains. The $CdCl_2$ has been etched[44].

Salavei et al. also showed that increasing the concentration from 10 mbar of HCF_2Cl diluted in 50 mbar of Ar to 10 mbar of pure HCF_2Cl resulted in less recrystallization as seen in Figure 1.13. This trend is somewhat counterintuitive.

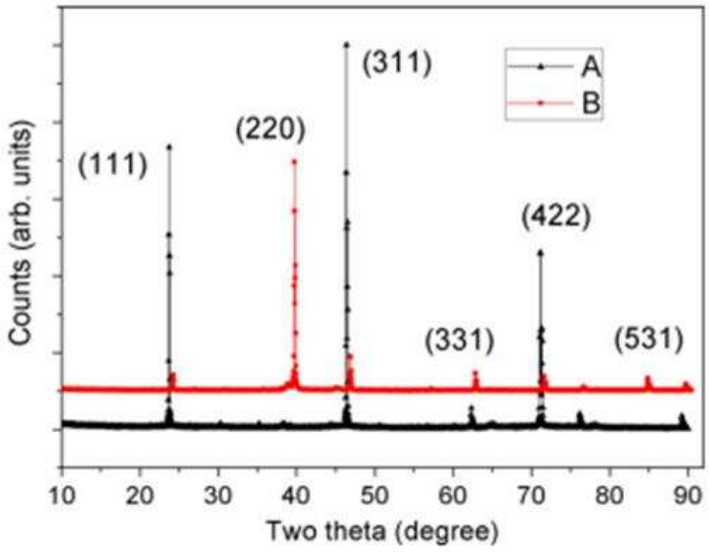

Figure 1.13 XRD data for (A) 10 mbar HCF_2Cl/50 mbar Ar and (B) 10 mbar HCF_2Cl[44].

A partial pressure of 50 mbar HCF_2Cl in 400 mbar Ar, a time of 5 min, a temperature of 400 ºC, and no oxygen gave Vaillant et al. a 14.8 % efficient device with V_{oc} = 820 mV, FF = 69 %, and J_{sc} = 26.2 mA cm^{-2}. Interestingly, Rios-Flores et al. required oxygen during the treatment similar to a conventional $CdCl_2$ activation to obtain an optimized 14 % efficient device with V_{oc} = 828 mV, FF = 69 %, and J_{sc} = 26.2 mA cm^{-2}. Other than the oxygen content the conditions were similar: 50 mbar HCF_2Cl in 400 – 800 mbar of a O_2/Ar mix, 400 ºC, and 5 min. It is possible that oxygen was needed during the treatment because CdS was deposited in pure Ar while Vaillant et al. deposited CdS in a 90 % Ar and 10 % CHF_3 ambient. The CHF_3 may have limited CdS consumption during the activation step, which is a common role of oxygen and therefore did not require any presence of oxygen for optimization. Although quality devices have been obtained with a HCF_2Cl treatment, this method is still undesirable because HCF_2Cl is linked to ozone depletion and its usage is restricted.

Another studied alternative to $CdCl_2$ is using HCl vapor or dry gas [45]. Qu et al. initially investigated HCl vapor treatments by bubbling Ar through a 25 Mol % solution but decided to switch to dry HCl gas diluted in Ar after equipment failure due to HCl vapor exposure. Grain growth was observed by SEM images when the HCl/Ar concentration was increased from 0 – 5 % during a 30 min activation at 400 ºC and also when the temperature increased from 380 – 440 ºC. The (111) texture coefficient decreased an as-deposited TC_{111} = 4-7 to TC_{111} = 1.2 when the HCl concentration was increased from 0 -5 %. These microstructural and morphological changes indicate that HCl can be an effective fluxing agent, similar to $CdCl_2$. Using a HCl concentration of 5 %, a treatment temperature of 400 C, and a time of 30 min resulted in ~ 8 % devices.

Non-cadmium containing salts have also been investigated for $CdCl_2$ alternatives and include $MgCl_2$, NH_4Cl, NaCl, HCl, KCl, and $MnCl_2$[46, 47]. The performance results for these alternatives are shown in Table 1.1 and indicate that $MgCl_2$ and NH_4Cl can be used as replacements for a solid-vapor activation treatment. These electrical properties were correlated strongly with microstructural changes quantified by texture coefficients. The greatest extent of recrystallization resulted in the best efficiency, which was the case for the $CdCl_2$ treatment. As seen in Table 1.2, the ranking in efficacy of each alternative is correlated with a reduction in TC(111). These results are important because they show that in order for an activation alternative to be successful, significant recrystallization must occur as indicated by a reduction in

Table 1.1 Performance results for device activated with non-cadmium containing salts[47].

Table 1.1 Performance results for device activated with non-cadmium containing salts[47].

	Efficiency [%]	Open-circuit voltage [V]	Short-circuit current [mA cm^{-2}]	Fill factor [%]
$CdCl_2$	13.02	0.831	22.13	70.01
$MgCl_2$	12.71	0.821	22.41	69.08
NH_4Cl	10.31	0.804	22.02	63.29
HCl	8.24	0.700	20.37	57.80
NaCl	6.75	0.603	19.78	53.34
KCl	5.49	0.607	17.95	50.11
$MnCl_2$	4.37	0.520	18.30	45.87

Table 1.2. Texture coefficients for various activation salts at optimal conditions [48].

	As-grown	$CdCl_2$	$MgCl_2$	NaCl	NH_4Cl
C_{111}	3.02	1.86	1.92	3.42	2.40
C_{220}	0.16	0.60	0.24	0.24	0.17
C_{311}	0.72	1.25	1.40	0.65	0.94
C_{400}	0.87	0.74	0.76	0.51	1.01
C_{331}	0.47	0.75	0.56	0.56	0.59
C_{422}	0.75	0.79	1.10	0.61	0.89
σ	0.93	0.43	0.55	1.10	0.69

TC(111). If TC(111) does not approach a value of 1 after activation, significant strain the p-n interface, defect densities, etc. degrade performance of devices. Bond dissociation energies also correlate to efficiencies between salts because a lower bond energy allows for greater Cl dissociation and greater recrystallization (3 - 4 eV for $CdCl_2$, $MgCl_2$, and NH_4Cl with > 4 eV for NaCl). Although these alternatives are non-toxic and produce devices that are comparable to the $CdCl_2$ activation, they are solid materials that have solid-vapor equilibrium which necessarily couples concentration and temperature during processing. As previously discussed, this property causes run-to-run variation and makes control difficult during activation.

The common element between the above mentioned alternatives is Cl, which has led to one group reporting on the use of Cl_2 gas as an activation agent [48]. In their report little information is given on the experimental conditions or film properties, but 9 – 10 % devices were obtained with exposure to a Cl_2/N_2 flow. Cl_2 is particularly encouraging because it does not contain cadmium, allows for precise gas phase delivery of Cl, and is an inexpensive source that is commercially available at a wide

range of concentrations at high purities. It is the scope of this thesis to explore the parameter space of an alternative activation treatment using molecular chlorine using microstructural and electrical characterization techniques. Goals for the activation treatment will be to determine if cadmium is required for highest efficiency devices, determine the most efficient conditions, and evaluate device performances. Additionally, the microstructural, morphological, electrical, and optoelectronic properties of a Cl_2 activated device will be compared with a $CdCl_2$ standard.

CHAPTER 2

EXPERIMENTAL METHODS

The information contained in Chapter 2 primarily consists of the experimental methods that were used throughout the course of research used in this thesis. It provides information on device fabrication and characterization conditions.

2.1 Substrate Preparation

Fabrication of superstrate CdTe devices began with proper cleaning of a TEC 15 (TCO/glass) substrate. TCO/glass substrates are generally characterized by the sheet resistance and visible light transmittance of the TCO layer, and for TEC 15 the TCO layer is ~200 nm of fluorine-doped tin oxide, giving a sheet resistance of <15 Ω/sq. and ~82 % light transmittance. Commercially available TEC 15 glass, at a thickness of 3.2

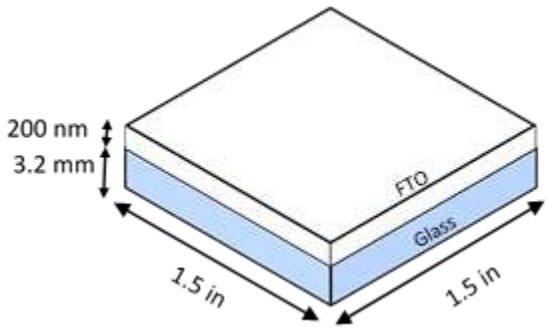

Figure 2.1 Schematic diagram of TEC 15 glass

mm, was cut into 1.5” x 1.5” squares with sample identification marks made via a precision diamond scribe. After cutting the glass, the surface of the TEC 15 substrates were cleaned by scrubbing both the FTO coated and glass surfaces with an alkaline cleaning concentrate (Micro-90®) soaked Kimwipe® for ~30 s followed by rinsing with

deionized water. After the deionized water rinse, it was found that blow drying first the glass side followed by the TCO side of the substrates resulted in less water droplet residue on TCO side, and a more uniform window layer could be deposited. The final step in the substrate cleaning process consisted of a 25 min exposure in an UV/ozone cleaner. The time between UV/ozone exposure of TEC 15 substrates and subsequent window layer deposition was always minimized at around 5-20 min, and it never exceeded more than 1 hour.

2.2 CdS Thermal Evaporation

After proper cleaning of FTO substrates, a 150 nm window layer of CdS was deposited onto the TCO in a thermal evaporator, shown in Figure 2.2. A diagram of the pumping and valve configurations of the system is given in Figure 2.3. The CdS source

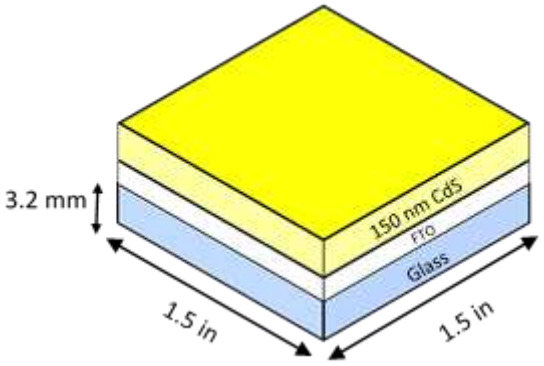

Figure 2.2 Glass/FTO/CdS stack

consisted of 99.999 % pure chunks contained in a tungsten boat. The thermal evaporator was equipped with a resistive substrate heater and a quartz crystal monitor (QCM), as seen in Figure 2.3, for control of the thickness and deposition rate of CdS films. The standard deposition consisted of pumping down the chamber to high vacuum (10^{-6} Torr) with a diffusion pump, backed by a rotary vane pump. A hot cathode

ionization gauge was used to measure high vacuum pressures, and a cold trap located at the inlet of the diffusion was filled with liquid nitrogen to obtain lower base pressures. Prior to connecting the diffusion pump to the chamber, the mechanical pump roughed the diffusion pump foreline and chamber to a base pressure of ~50 mTorr. Once a standard 150 ºC substrate temperature and HV was obtained in the chamber, approximately 60 amp of current was passed through the CdS containing crucible resulting in a ~5 Å/s deposition rate as measured by the QCM controller. The QCM was previously calibrated by depositing films and measuring thickness with contact profilometry. The shutter was opened after the desirable deposition rate was obtained for a total thickness of 150 nm. Up to four 1.5” x 1.5” substrates could be processed in the thermal evaporator per run, resulting in very uniform, transparent films. After removing the films from the substrate holder, no other cleaning techniques were performed before absorber deposition. Time was always minimized between CdS and absorber depositions with a maximum amount of elapsed time between depositions consisting of 4 hours.

2.3 CdTe Vapor Transport Deposition

After deposition of 150 nm of CdS a 3 – 4 µm thin film of CdTe was deposited by vapor transport deposition (VTD) at a substrate temperature of 420 ºC, 20 Torr nitrogen carrier gas, and 10? % oxygen (Figure 2.4). A real image and accompanying schematic diagram of the system are given in Figures 2.5 and 2.6, respectively, on the following pages. Differential heating is employed in the quartz source tube to vaporize solid CdTe

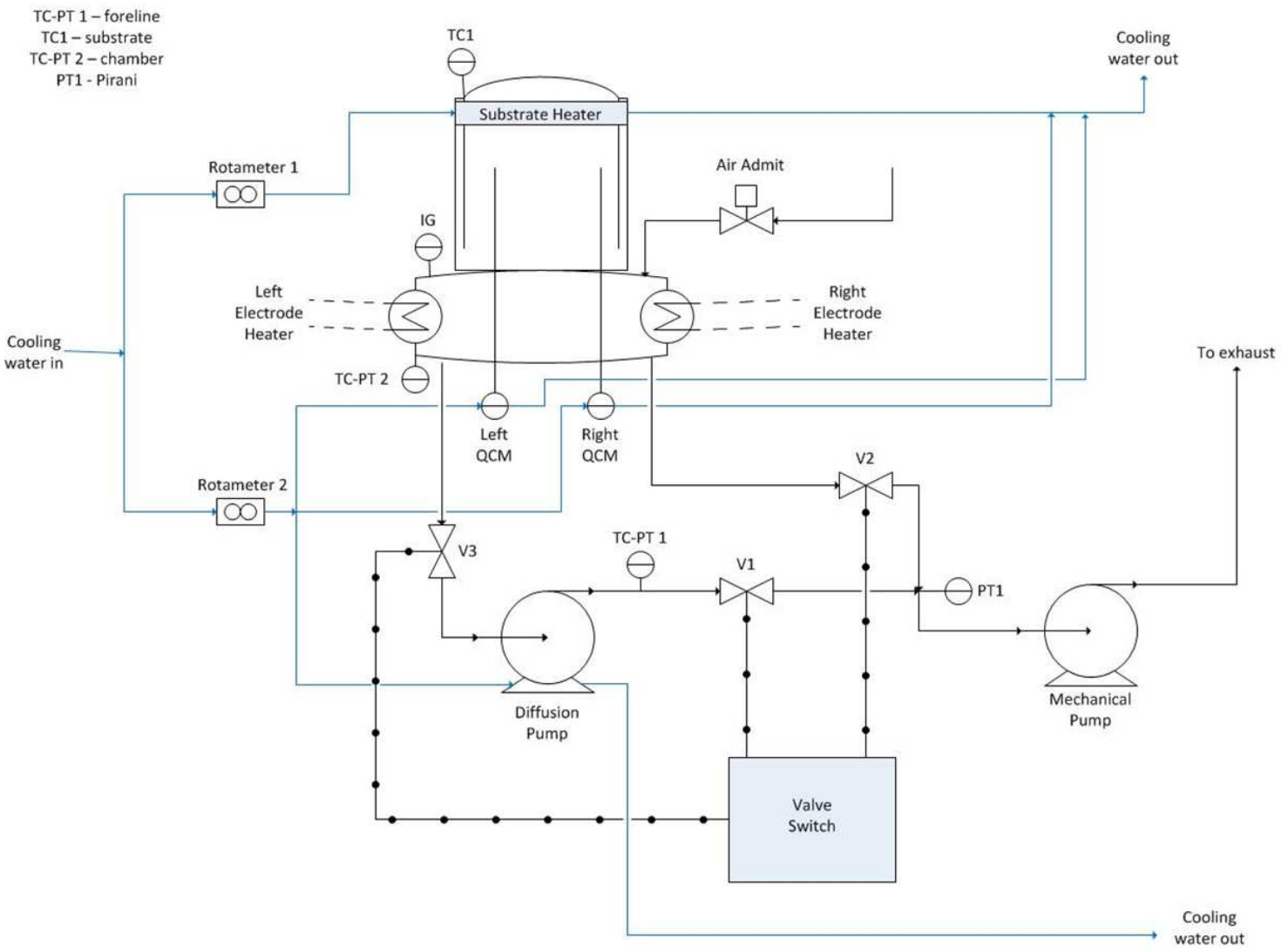

Figure 2.3 Thermal evaporator diagram

into a flowing stream of nitrogen and to ensure that only saturated Cd and Te_2 vapor pass through the porous frit.

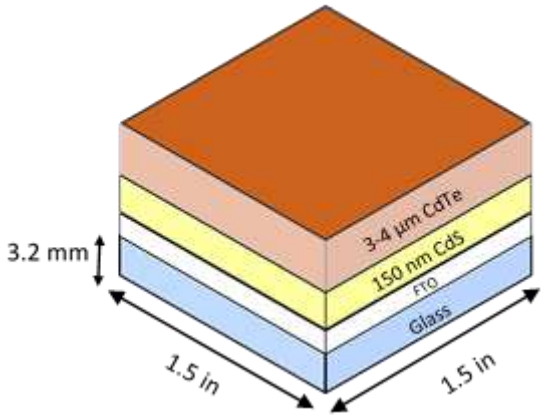

Figure 2.4 Glass/FTO/CdS/CdTe stack

This is accomplished by maintaining a temperature difference of at least 15 ºC between the source and frit radiative heaters. Typical operating temperatures were 650 ºC for the source and 670 ºC for the frit. A 1.5” x 1.5” substrate holder was spaced ~0.75” below the quartz frit, which was always heated to 420 ºC with a SiC heating element. A shutter between the frit and substrate holder was used to control deposition, and a convection gauge monitored pressure at the CdTe source. Nitrogen was delivered to the inlet of the source tube with an electronic mass flow controller at a rate of 375 sccm. Oxygen was delivered at the bottom of the deposition chamber at a tenth of the nitrogen flow (37.5 sccm). Small amounts of oxygen was found to be crucial to depositions because of advantageous material properties of deposited CdTe films in an oxygen ambient and because the NiCr alloy heaters of the source and frit would form a native oxide in the

presence of oxygen during the high operating temperatures, preventing fracture/failure of the heating wires during depositions.

A standard deposition consisted of pumping down the deposition chamber with a mechanical pump to ~360 mTorr and setting the temperature controller to 420 ºC for the SiC heating element located beneath the substrate holder. After approximately 30 min, the substrate would nearly reach its setpoint, and the temperature controllers for the source and frit would be set to ~650 ºC and ~670 ºC, respectively. Immediately following the switching of the source and frit temperature controllers, nitrogen and oxygen gas flow was introduced to the chamber, and a resulting base pressure of 20 Torr was measured without the use of throttling/conductance valves. Once the source, frit, and substrate heaters reached setpoints, the shutters were opened and a 3 – 4 µm deposition was performed. Deposition rates were calibrated using contact profilometry with rates better than 0.78 µm/min obtained. Although the 420 ºC substrate temperature was never changed, the source and frit temperature would gradually be increased in order to maintain the ~1 µm/min deposition rates. The maximum source temperature used was 675 ºC after approximated 50 depositions. At this point the source tube would need to cleaned with nitric acid and the CdTe source chunks replenished.

2.4 Chlorine Activation

Following the vapor transport deposition of CdTe, the as-deposited stacks were recrystallized by gaseous chlorine (Cl_2) activation. For comparisons and analysis, samples were also activated by the standard $CdCl_2$ treatment. The standard $CdCl_2$ consisted of a CSS type geometry in a 3 zone quartz tube furnace with up to four 1.5” x

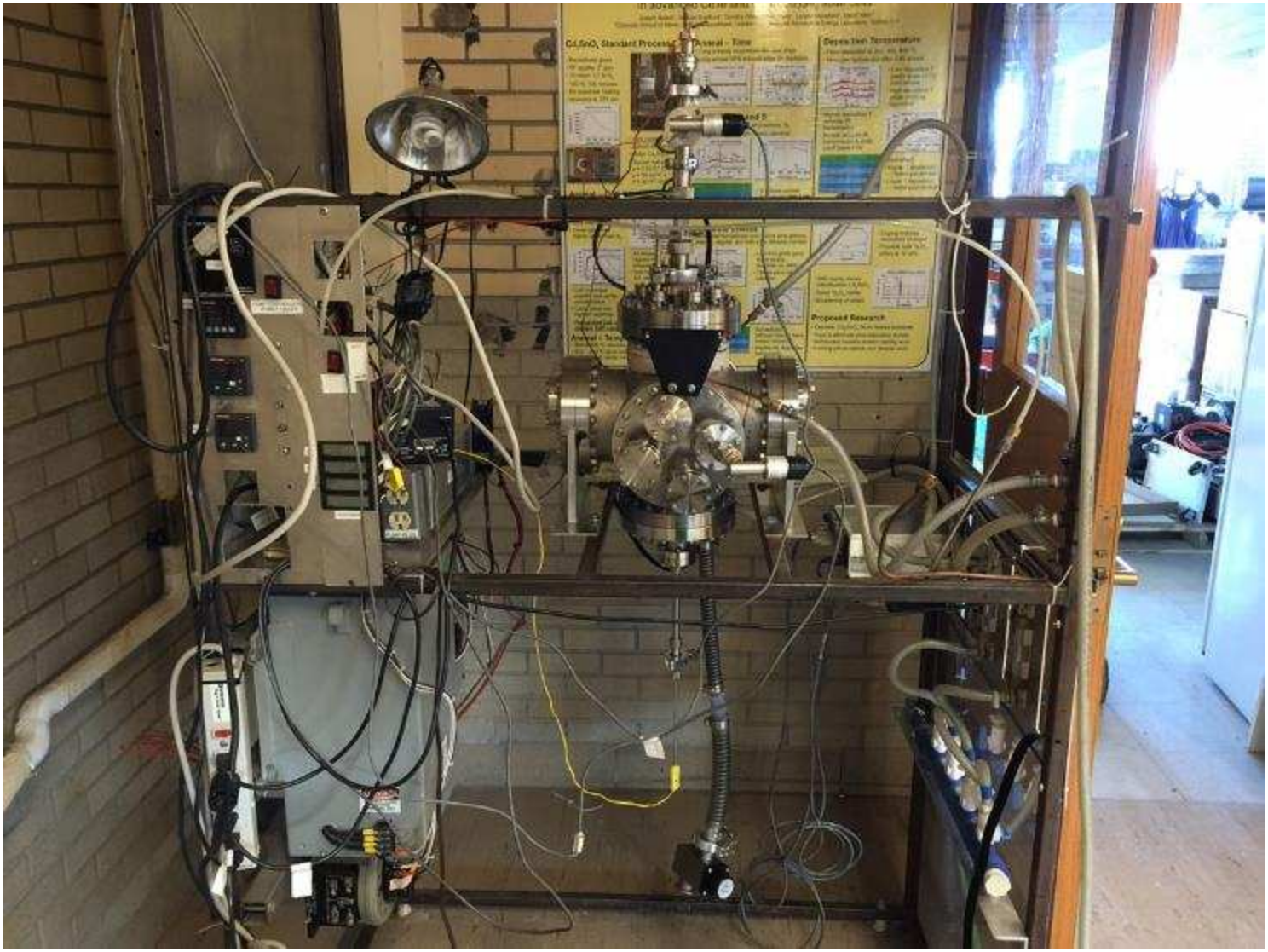

Figure 2.5 VTD System Image

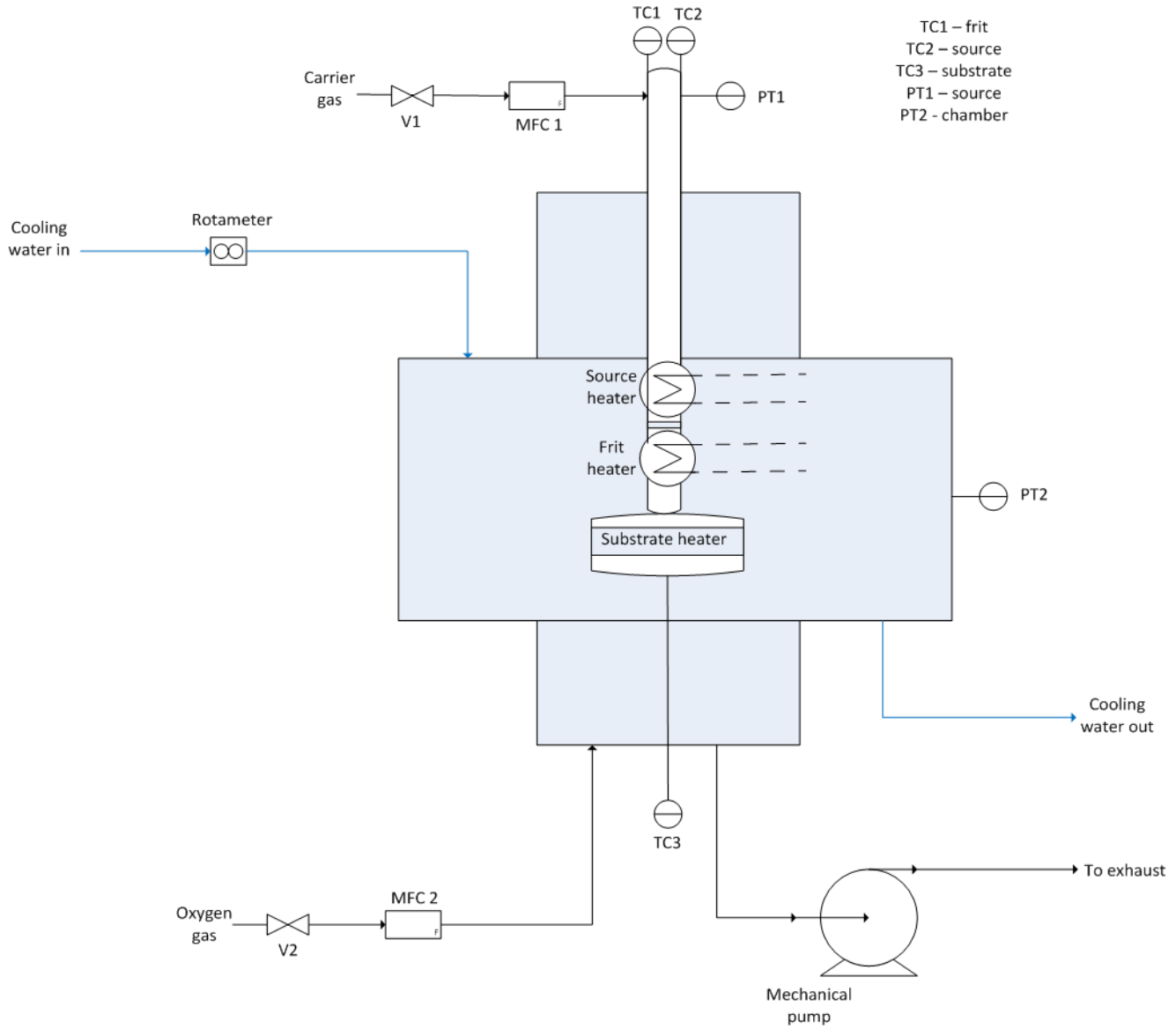

Figure 2.6 VTD Schematic Diagram

1.5” samples placed in a graphite holder that contained $CdCl_2$ chunks. Typical processing began by purging the quartz tube at atmospheric pressure in a 50/50 oxygen and nitrogen mixture at 2000 sccm for 20 min. After 20 min, the heaters were powered and the flow was reduced to 400 sccm while maintaining the 50/50 oxygen and nitrogen composition. Once the thermocouple positioned above the graphite crucible reached 400 ºC, 30 min would be allowed to elapse before the power to the heaters was switched off. The 400 sccm gas mixture would continue to flow until the furnace reached 290 ºC, at which point the samples were completely removed from the quartz tube and quickly cooled under ambient conditions to room temperature.

For the novel activation of the as-deposited glass/FTO/CdS/CdTe with gaseous Cl_2, a custom tube furnace was designed constructed and is schematically shown on the following page in Figure 2.7. All piping was constructed of 1/4” 316L stainless steel and the material construction of the tube was quartz. Table 2.1 indicates the specifications of the quartz tube which was enclosed by ceramic heating material. Mass flow controllers

Table 2.1 Quartz tube specifications.

Material	Outer Diameter (mm)	Wall Thickness (mm)	Length (mm)	Notes	Company
Quartz	50	3.3	610	rounded ends	ASG

(MFC) used to independently control flow of nitrogen, oxygen, and 3 % Cl_2/Ar to the furnace with maximum flow rates of 833 sccm, 300 sccm and 5 sccm, respectively. The 3 % Cl_2/Ar cylinder was equipped with a reactive gas regulator allowing for it to be either purged with another line of pure Ar or to be pumped down to rough vacuum with a

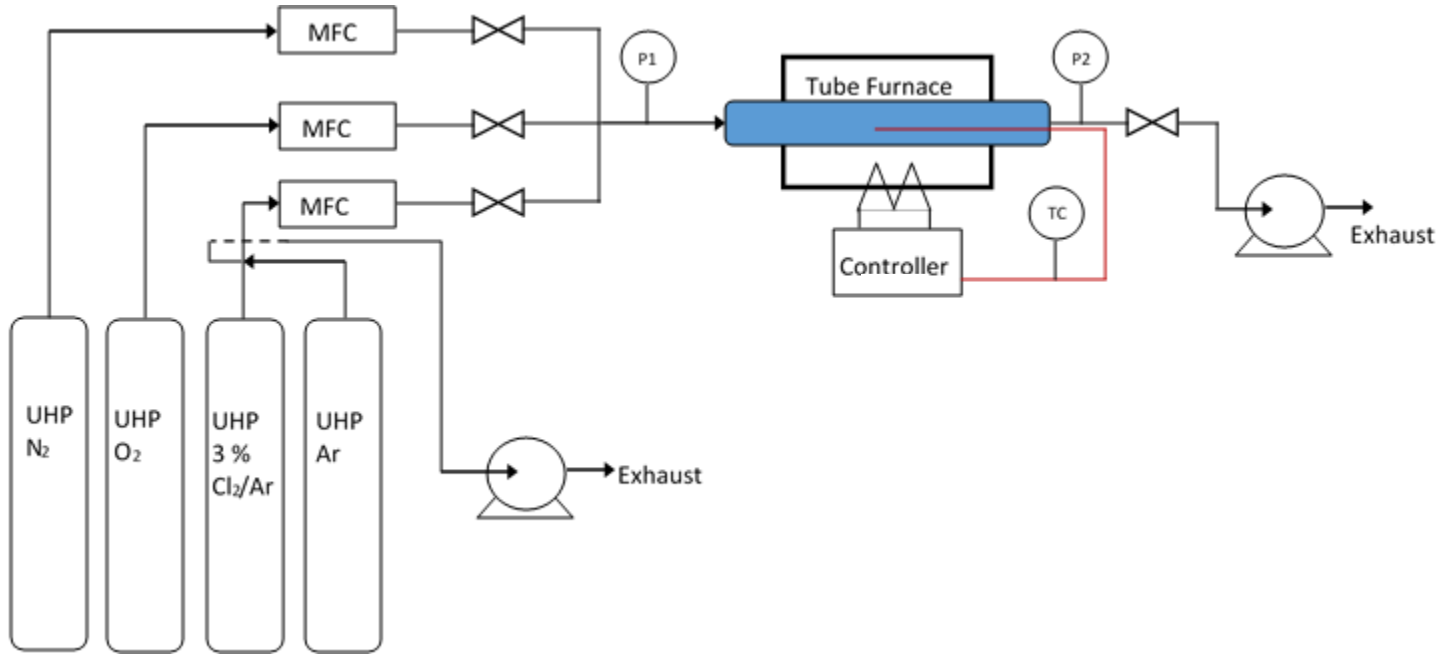

Figure 2.7 Cl_2 Tube Furnace

with a mechanical pump. The regular essentially was a four way valve allowing all possible connections between a pure Ar inlet, a 3 % Cl_2/Ar inlet, a rough vacuum, and a line to a furnace MFC. A thermocouple was inserted directly in the middle of the quartz tube. A needle valve downstream of the furnace allowed for modulation of conductance and was always adjusted until a system pressure of 600 Torr was found during full gas flow. After a substrate was loaded into the middle of the furnace, the tube was pumped down to ~100 mTorr with a mechanical pump followed by delivery of a set nitrogen/oxygen composition via the MFCs. Regardless of the composition of O_2/N_2 mixture, the total flow rate was always set to 800 sccm, and the initial base pressure before gas introduction was read with a 10 Torr capacitance manometer, seen as P1 in Figure 2.7. During this time the Cl_2 MFC connected to only pure Ar via the reactive gas regulator and was set to a desired flow rate. After initiating gas flow, the throttling valve was adjusted until a pressure of 600 Torr was read on a 1000 Torr capacitance manometer, as denoted by P2 in Figure 2.7, and the temperature controller was set to around 400 ºC. Once the temperature setpoint was reached, the pure Ar to the Cl_2 MFC and the valve in front of the MFC were closed. The vacuum line between the reactive gas regular and the mechanical pump was next opened, allowing for the line between the outlet of the Cl_2 MFC and the outlet of the 3 % Cl_2/Ar to be pumped down to rough vacuum. Once this was achieved, the vacuum line was closed off and the outlet of the 3 % Cl_2/Ar was opened. A timer was started after opening the valve in front of the Cl_2, constituting a t = 0 reaction time. After the reaction, the valve in front of the Cl_2 was closed and power to the heater was cut. The Cl_2 line was pumped down to rough vacuum with pure Ar being subsequently supplied to purge the reactive gas regulator

and any residual Cl_2 in the system. During cool down, the O_2/N_2 mixture at 600 Torr was allowed to keep flowing in addition to pure Ar through the Cl_2 MFC. At approximately 150 ºC, the substrate was removed from the quartz tube and cooled in ambient conditions. Table 2.2 summarizes the various conditions of the tube furnace that were studied throughout the duration of the research.

Table 2.2 Studied conditions of Cl_2 tube furnace

Temperature (°C)	3 % Cl_2/Ar Flowrate (sccm)	O_2/N_2 Composition (%)	Time (min)	Pressure (Torr)
380 - 420	0 - 5	0 - 25	0.5 - 10	600

2.5 ZnTe:Cu Contacts

After the Cl_2 or $CdCl_2$ activation step, a cleaning procedure occurs where the sample is completely immersed in a 0.05 % Br_2/methanol (200 mL MeOH + 0.1 mL Br_2) solution under gentle agitation for 10 sec followed by a pure MeOH rinse. Elemental halogens and their solutions etch II-VI compounds, and as a result, this cleaning removes oxide precipitates and causing Te excess, yielding an increased p-type conductivity at the exposed surface of the CdTe layer which is important for creating ohmic contacts.

Once the substrates are removed from the MeOH rinse, the samples were allowed to air dry for ~10 min before being placed in a thermal evaporator for deposition of a 150 nm film of ZnTe:Cu onto the 3-4 µm of CdTe, as shown in Figure 2.8(a). The deposition occurred in the same system as one used for CdS deposition but another set

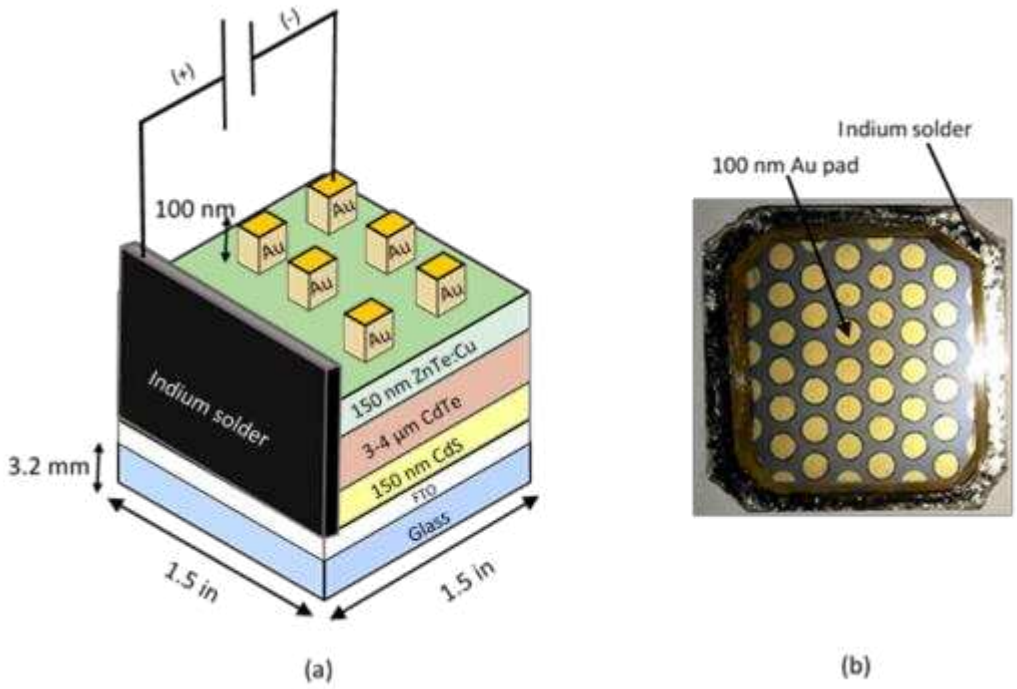

Figure 2.8 Schematic of completed devices (a) and corresponding image of completed devices (b)

of electrodes was employed in order to perform co-evaporation from 99.999 % pure Cu in one set and 99.999 % pure ZnTe in another. A baffle was placed between the two sets of electrodes allowing for two QCMs to measure and independently control deposition rate of pure Cu and ZnTe (Figure 2.9). The substrate temperature was set to 100 ºC and a 10^{-6} Torr high vacuum was used, similar to the CdS depositions. Because ZnTe has a significantly lower pressure, the maximum deposition rate as measured by the QCM was always obtained with the Cu deposition rate being accordingly set to 10 % of this value. A typical maximum deposition rate for ZnTe was ~1.5 Å/s at ~50 amp, thus the typical Cu deposition rate was 0.1 Å/s at ~80 amp. Regardless of deposition rates,

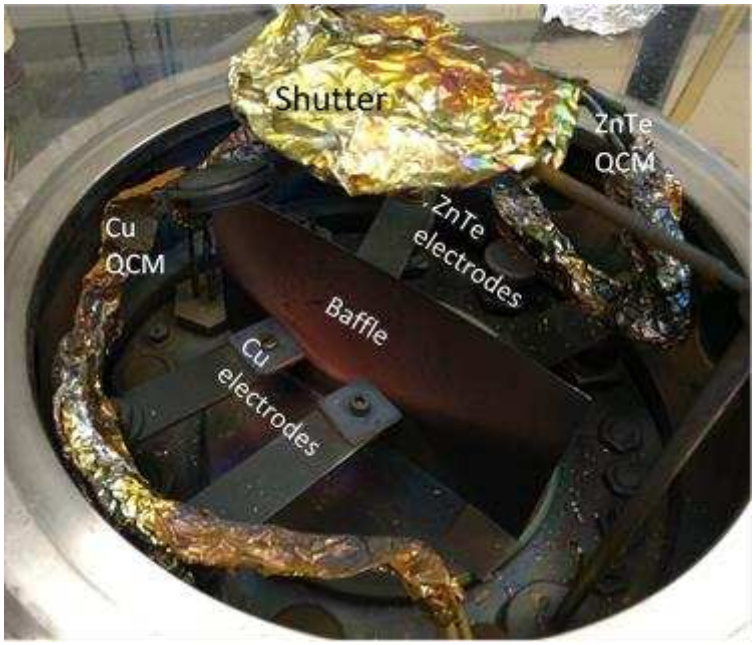

Figure 2.9 Addition of a baffle for thermal co-evaporation.

the shutter was closed when ZnTe and Cu films grew to 150 nm and 10 nm, respectively. Immediately following the closing of the shutter, the power to the two sets of electrodes and substrate heater was removed. 100 nm metallization layers of Au pads were subsequently evaporated in the same system onto the ZnTe:Cu film using a shadow mask and are schematically shown in Figure 2.8(a). Each Au pad had an area of 0.079 cm^2 and defined the area for each device on the ZnTe:Cu film. The standard Au deposition rate was ~5 Å/s at ~80 amperes. Following the deposition of Au pads, a diamond tipped scribe was used to scribe around each gold dot down to the FTO, resulting in electrically isolated 0.079 cm^2 devices. A razor was used to remove material around the edges of the 1.5” x 1.5” sample down to the FTO after which indium was applied to the exposed front contact with a soldering gun, shown schematically in Figure 2.8(a) and as a real image in Figure 2.8(b).

Following the application of indium to the front contact and scribing devices, rapid thermal processing (RTP) was employed to activate the back contact by optimizing the diffusion of Cu into the ZnTe and CdTe layers. The RTP system consists of a ceramic substrate holder, radiative heaters, injection of Ar gas, and a mechanical pump. Images of the system are shown in Figure 2.10. The standard process began by pumping down the volume to rough vacuum followed by Ar delivery at ~30 Torr. Once a stable flow rate was obtained, the temperature trajectory was programmed. Every sample underwent a standard room temperature to 320 ºC ramp in 20 s followed by a 30 s dwell at 320 ºC. Once the system was at 200 ºC, another 20 s ramp and 30 s dwell at 330 ºC was programmed. After the sample cooled to 200 ºC under 30 Torr of Ar flow, the sample was removed and cool to room temperature. The RTP treatment is the final

Figure 2.10 Rapid Thermal Processing (RTP)

processing step in the fabrication of CdTe solar cells and allows for probes to be connected to the front and back contacts for electrical measurements.

2.6 X-Ray Diffraction

X-ray diffraction (XRD) a powerful, non-destructive technique that gives phase and microstructural information of thin films by measuring properties such as grain size, lattice spacing, lattice strain, dislocation density, alloying, film texture, crystallinity, surface structure, etc. Diffraction of X-rays occurs when the wavelength of the incident electromagnetic waves becomes comparable to the interatomic distances that are perpendicular to the thin film surface, resulting in the constructive interference of the waves at angles specified by Bragg's law:

$$\lambda = 2d_{hkl} \sin\theta \qquad (2.1)$$

where λ is the wavelength (Å) of the radiation, d_{hkl} is spacing (Å) of a family of parallel (hkl) atomic planes, and θ (degrees) is the angle of incidence of the X-ray. Bragg's law can be derived from basic geometry as seen in Figure 2.11:

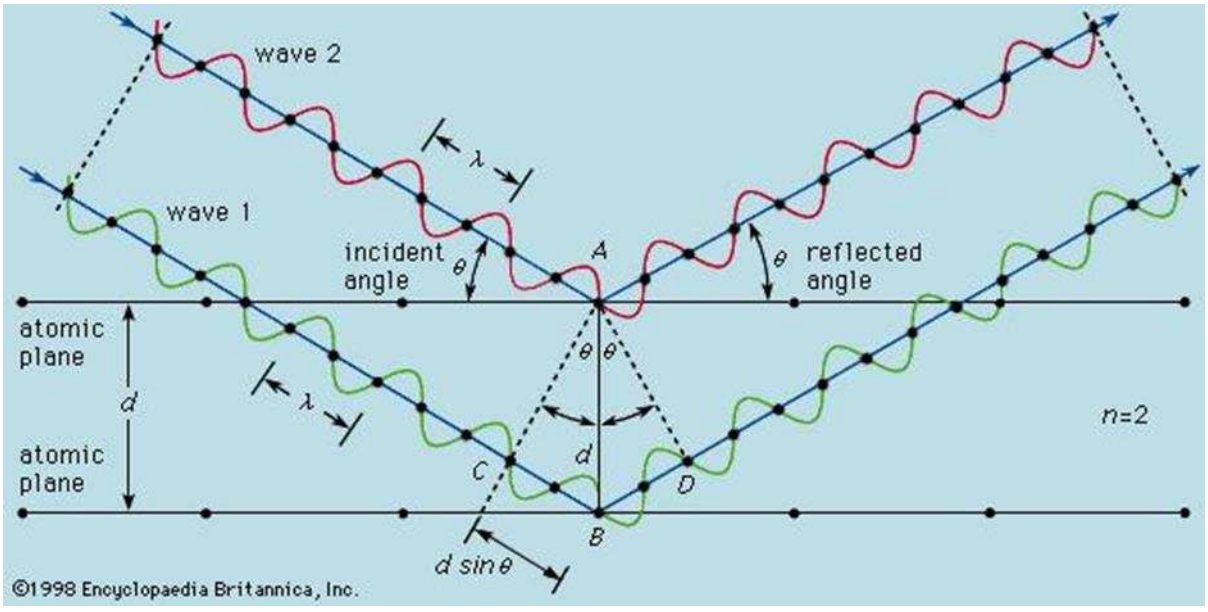

Figure 2.11 Bragg's Law

X-ray diffractometers generally consist of an X-ray source, incidental angle optics, a goniometer, and detection optics, resulting in a plot of intensity vs.θ. Analysis of the resulting peak intensities, Bragg angle location, full width at half maximums, d-space, and integrated areas provides insight into the above mentioned properties of thin films. A copper anode was used as a source for scans of all samples using Cu Kα radiation at λ = 1.54 Å. Wide angle scans in the 2θ range of 20 - 80º were taken for all samples that underwent texture coefficient analysis with an increment of 0.05º at a dwell time of 1 sec.

As previously mentioned, the texture coefficient is a measure of the orientation of grains and extent of recrystallization in polycrystalline CdTe films. The texture coefficient was used as an indicator of how much recrystallization took place when variables such as oxygen concentration, chlorine concentration, temperature, and time were varied and these values were compared against the extent of recrystallization of a standard $CdCl_2$ activated sample for insight. To start off the texture coefficient analysis, a 20 - 80º/0.05/1sec 2θ was taken, as shown in Figure 2.12 on an activated glass/FTO/CdS/CdTe stack after a 10 s Br/MeOH etch. Only the 7 planes allowed for cubic zincblende CdTe in this 2θ range are indexed and used during the texture coefficient analysis of samples. All other planes, due to oxides and TCO, show low intensities and are neglected in the CdTe texture coefficient analysis. The intensities are normalized by the (111) plane in Figure 2.12 for clarity, but it is the measured intensities (height) which are used during the analysis. After each scan, software was used to subtract the background by fitting a cubic spline function and the Cu $K\alpha_2$ doublets were

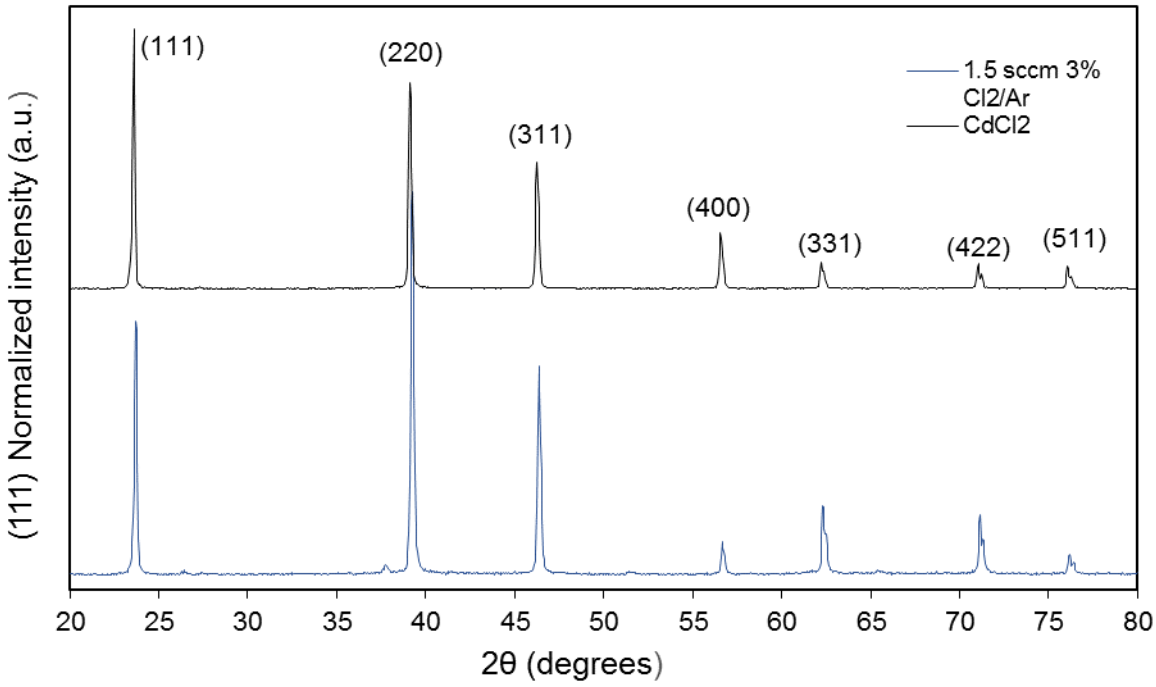

Figure 2.12 Standard 20 – 80º XRD scans of activated samples

Table 2.3 Post-processed XRD data suitable for TC analysis

	2-Theta	d(Å)	Height	H%	Area	A%	FWHM
1.5 SCCM 3% Cl_2/Ar	23.694	3.752	1822	57.6	343.6	59.1	0.16
	39.208	2.2959	3162	100	581.5	100	0.156
	46.347	1.9575	1789	56.6	309.2	53.2	0.147
	56.664	1.6231	290	9.2	45.5	7.8	0.134
	62.317	1.4888	628	19.9	117.1	20.1	0.158
	71.141	1.3242	541	17.1	99	17	0.155
	76.177	1.2487	179	5.7	33.1	5.7	0.157
$CdCl_2$ Activated	23.581	3.7698	4071	100	752.9	100	0.157
	39.095	2.3022	3849	94.6	650.6	86.4	0.144
	46.24	1.9618	2379	58.4	415.4	55.2	0.148
	56.553	1.626	1154	28.4	198.2	26.3	0.146
	62.216	1.4909	561	13.8	106.2	14.1	0.161
	71.042	1.3258	519	12.8	94.6	12.6	0.155
	76.061	1.2503	457	11.2	92.2	12.2	0.171

removed. The software also used statistical methods to fit each peak and determine the Bragg angle location, height, FWHM, and area. An example final, post-processed data that is suitable for texture coefficient analysis is given in Table 2.3. The texture coefficient (TC) was calculated according to the following equation:

$$TC(111) = \frac{I(111)}{I_0(111)}\left(\frac{1}{n}\sum_{n=1}^{7}\frac{I(hkl)}{I_0(hkl)}\right)^{-1} \qquad (2.2)$$

where TC(111) gives the TC of the (111) plane for the polycrystalline film, I(111) is the as-measured intensity for the (111) plane, $I_0(111)$ is the reported (111) intensity from a standard powder diffraction file (PDF). In the denominator of the expression, a summation of the measured intensity I(hkl) normalized by the corresponding PDF intensity $I_0(hkl)$ is performed over the remaining observed Bragg planes in the 2θ scan for a particular phase, where n is the total number of observed Bragg planes used in the calculation. The variable n is always equal to 7 for the presented TC analyses. As a result of a few mathematical constraints, several useful conclusions can be drawn from the value of the (111) texture coefficient. If the all of the grains are oriented along the (111) plane the only measured intensity is from (111), and TC(111) = 7 because the denominator becomes $1/7*[I(111)/I_0(111) + 0 + 0 + 0 + 0 + 0 + 0] = 1/7*[I(111)/7I_0(111)]$ and the numerator becomes $I(111)/I_0(111)$. A value of TC(111) = 7 after a Cl_2 indicates that no recrystallization took place during the treatment because as-deposited films generally give TC(111) = 7. If TC(111) = 1, the grains in the film have become perfectly randomly oriented because all (hkl) planes have intensities equal to their PDF values. Thus, in the range 1 < TC(111) < 7 a relative measurement of the extent of

recrystallization between samples can be determined. If TC(111) < 1, the film has some degree of preferential orientation along another (hkl) plane.

2.7 Solar Simulator

The basic equations and operating principles of a solar simulator were outlined in the introduction, and the basic equipment used for testing of fabricated cells was obtained from a commercially available solar simulator. The system was fully automated and tested cells under standard AM 1.5 illumination. A basic circuit of a general solar simulator consists of a DC voltage source, AM 1.5 source, an oscilloscope, a programmable multimeter, and a computer equipped with a control software. Essentially, the multimeter measures the voltage drop across the solar cell and the amount of current for a given applied DC voltage while under AM 1.5 illumination. The computer performs automated electrical and calibration calculations resulting in a characteristic I-V curve per “flash” of AM 1.5 illumination. Two wires constitute probes with one connected to the front contact and the other to the back contact. On the commercial system, a reverse to forward sweep direction was performed in the voltage range of -2 to 1 V at a source irradiance of 100 mW/cm^2. As part of the automation, the V_{oc}, J_{sc}, FF, and η would automatically be tabulated in addition to the characteristic J-V curve.

CHAPTER 3

Results and Discussion

This chapter represents the majority of results obtained throughout the duration of the research and has been adapted from work that is currently in preparation for submission to the 43rd IEEE Photovoltaic Specialists Conference, Portland, OR 2016.

3.1 Activation of CdTe Solar Cells Using Molecular Chlorine

Abstract — There has been renewed interest in developing alternatives to $CdCl_2$ activation, a critical but expensive step in CdTe manufacturing. A common element among the alternative agents that have been explored is chlorine, which facilitates recrystallization, passivates grain boundaries, and leads to enhanced efficiency. In this paper we present an evaluation of molecular chlorine (Cl_2) for CdTe activation. The broad process space was first screened by evaluating the change in the (111) texture coefficient. It is shown that recrystallization occurs quite quickly (~1 minute), and the required concentration of Cl_2 is quite low (<100 ppm). Devices fabricated at promising conditions displayed good rectification with device efficiency greater than 11%.

3.2 Introduction

A critical step in CdTe solar cell production is its activation through exposure to $CdCl_2$. This process results in recrystallization, grain growth, and interdiffusion with the CdS window layer [31, 32]. It has been shown that during this process Cl rapidly diffuses

through the film, preferentially accumulating in the CdS window layer and decorating CdTe grain boundaries [33, 34]. The original process involved exposing CdTe to a $CdCl_2$ solution through either immersion or spray application, followed by subsequent annealing at T ~ 400 ºC [49]. Early industrial practitioners realized the limitations of solution processing and moved to vapor phase exposure via $CdCl_2$ sublimation [48]. $CdCl_2$ activation is capital expenditure (Capex) intensive and has been described as the “the most intricate process in manufacturing” [50]. It would be desirable to simplify this aspect of CdTe manufacturing

Due to the complications described there has been a long history of exploring alternative to $CdCl_2$ which include HCl [45], chlorofluorocarbons [44, 43], and more recently non-toxic salts such as $MgCl_2$ [46, 47]. The common element among these reagents is chlorine, and in fact there is one report describing the use of Cl_2 directly [48]. In that study Cl_2 diluted in N_2 was used, and it was found that the resulting films were highly non-uniform due to etching, though isolated devices with efficiency in the range of 9-10% were reported. Little information was provided on the conditions explored but the authors concluded that Cl_2 was a viable candidate to fulfill standard production requirements such as yield, throughput and safety, but further optimization is required [48]. In this work we report our preliminary results to address this goal. XRD texture coefficient analysis [47] is used to first screen the large process space, and then promising conditions are used for device fabrication and compared with those produced by standard $CdCl_2$ activation.

3.3 Experimental

CdTe solar cells were fabricated on commercial fluorine-doped tin oxide coated glass superstrates (TEC-15). The standard device architecture consisted of 150 nm of evaporated CdS, ~4 microns of CdTe deposited by vapor transport deposition, and an RTP-activated back contact that employed a Cu-doped ZnTe buffer layer and gold metallization of 0.079 cm^2 pads [37]. The standard activation process employed exposure to $CdCl_2$ vapor in a close spaced sublimation geometry in a tube furnace at 400 ºC for 30 min using a 50%-50% O_2/N_2 ambient. Cl_2-activation was carried out in a quartz tube (50 x 610 mm) furnace initially evacuated by a mechanical pump. Small amounts (1-5 sccm) of a 3% (v/v) mixture of Cl_2 in Ar were further diluted with a mixture of N_2 and O_2. For each experimental trial, the total flowrate of N_2 and O_2 was maintained at 800 sccm, regardless of the partial pressure of each component. All gasses were delivered using electronic mass flow controllers, and for each treatment the tube furnace was maintained at 600 Torr using a throttling valve. The sample was heated to the desired setpoint with only O_2 and/or N_2 flowing. The duration of the experiment is based on the time Cl_2 was flowing through the system. The experimental conditions examined were Cl_2/Ar flowrate (1 – 5 sccm), temperature (375 – 420 ºC), oxygen concentration (0 – 25 %), and treatment time (0 – 10 min). X-ray diffraction (XRD) measurements were taken from 2θ = 20 – 80° using Cu K α radiation (Rigaku). Devices were scribed and solar cell performance was measured under simulated AM1.5 radiation using a commercial tool (PV Measurements) and external quantum efficiency (EQE) was measured on a custom system. Both were calibrated using a certified silicon standard.

3.4 Results and Discussion

A well-known consequence of $CdCl_2$ activation is CdTe re-crystallization [31], which was quantified using XRD texture analysis [47]. Equation (3-1) was used to quantify the (111) texture coefficient (TC)

$$TC_{111} \equiv \frac{I(111) \big/ I_o(111)}{\frac{1}{n}\sum_{n=1}^{7} I(hkl) \big/ I_o(hkl)} \qquad (3.1)$$

where I and I_o are the experimental and powder pattern intensities, respectively. JCPDS no. 15-0770 was the reference pattern used. A TC value of one indicates that a film has completely randomly oriented grains. Values greater than unity indicate preferential texturing in that orientation, while values <1 indicate texturing in another direction. As-deposited CdTe is highly textured in the (111) orientation with a TC value of 5-6, and this value is reduced below unity after $CdCl_2$ activation. Since re-crystallization is a necessary (but perhaps not sufficient) for high performance, this parameter was used to efficiently screen the process window without the need to complete full device fabrication.

The first parameter evaluated was temperature, with other parameters fixed at t = 10 minutes, 5 sccm Cl_2/Ar, and 25% O_2. Figure 3.1a displays raw XRD and 3.1b shows the resulting TC(111). The re-crystallization process is highly activated, with partial re-crystallization observed at T< 400 ºC, while films processed at T ≥ 400 ºC displayed TC(111) values very similar to conventional $CdCl_2$. Interestingly the threshold temperature of 400 ºC is near that reported most commonly for both standard $CdCl_2$ and

other alternatives, suggesting that this value is primarily a function of CdTe itself and not the specific activation agent employed. Based on these results the temperature was set to 400 ºC for further screening.

The second parameter evaluated was the Cl_2 flowrate and the results are shown in Figure 3.2 with parameters held at T = 400 ºC, 25 % O_2, and 10 min. It is found that insignificant re-crystallization is obtained at 0.5 sccm, but at higher values the TC was similar to standard $CdCl_2$. Note that control of flowrates at values < 1 sccm were questionable as it approached the limits of the instrument. Coincidentally, at 1 sccm the Cl_2 partial pressure in the reactor was 22.5 mTorr, very comparable to the vapor pressure of $CdCl_2$ at 400 ºC (~12 mTorr). So similar to temperature, there may be a threshold level of chlorine availability that is independent of the source of chlorine used. Based on these encouraging results a series of devices were fabricated as a function of Cl_2/Ar flowrate. Representative J-V curves and box plots summarizing device efficiency are shown in Figure 3.3. The performance of 10 devices from an individual sample were used to calculate the boxplot parameters for each flowrate, where the red line is the median efficiency, the blue lines represent the 25 % and 75 % quantiles, the black horizontal lines show the range of the set, and red crosses are statistical outliers. Device efficiency declines monotonically from 8 to 3% as the Cl_2 flowrate was increased from 1 to 5 sccm (Fig. 3.3b). Device uniformity is also reduced. Inspection of the JV curves reveals that there are declines in all secondary parameters, but the most prominent decline is in the open circuit voltage (V_{oc}) which drops from 694 to 368 mV. There is also a ~15% decline in the short circuit current density (J_{sc}) over the range explored. These results clearly indicate that Cl_2 is being provided in excess. Further

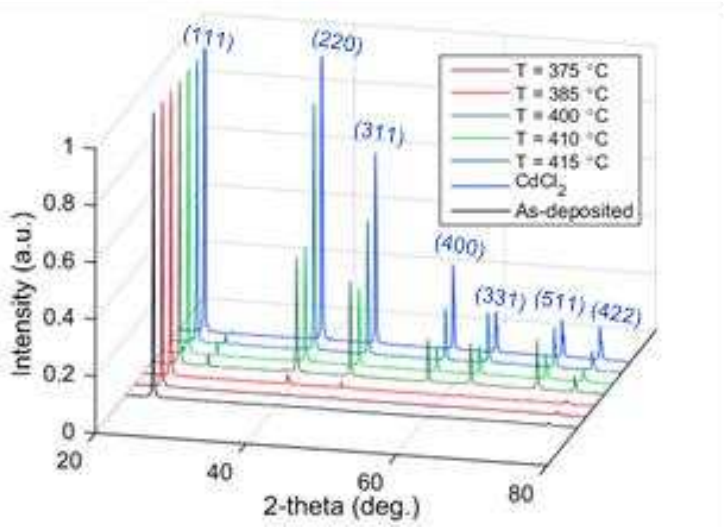

(a)

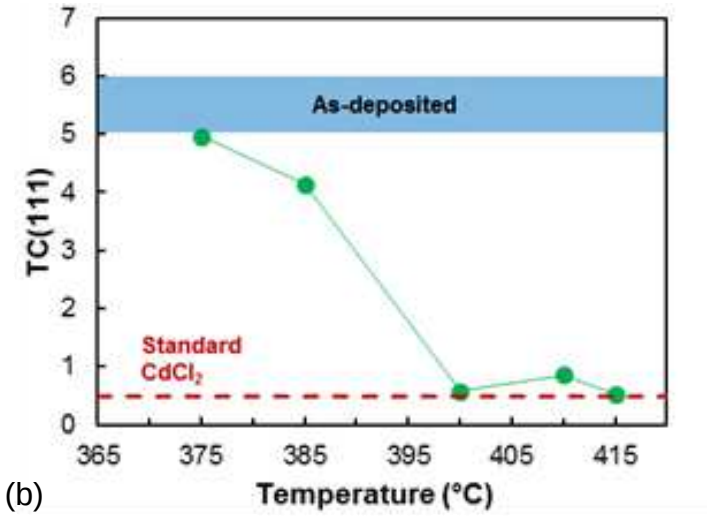

(b)

Figure 3.1 (a) normalized XRD patterns and (b) resulting (111) texture coefficient as a function of process temperature at t = 10 min, 25% O_2, 5 sccm Cl_2/Ar.

reductions in the Cl_2 density could not be achieved with the current experimental facilities, but work is underway to extend the range. The Cl_2/Ar flowrate was set 1.5 sccm for the remainder of the work presented here. As shown in Figure 3.3b, 1 sccm appeared to be the optimum, but there was not a significant difference between 1 and 2 sccm. Since 1

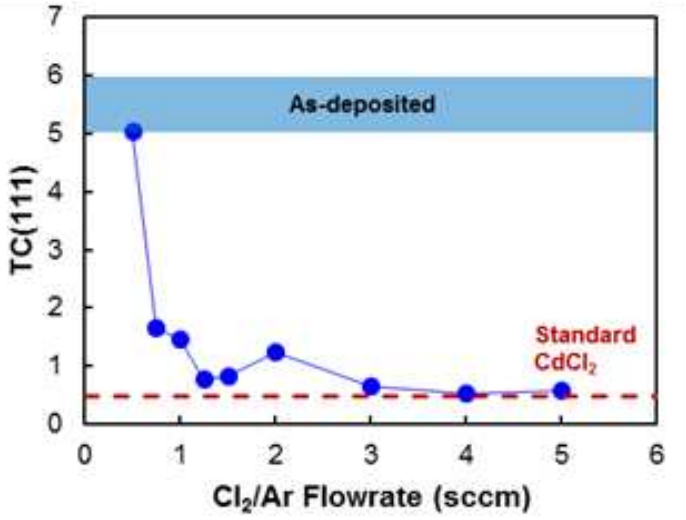

Figure 3.2 TC(111) as a function of Cl_2/Ar flowrate at T = 400 ºC, t = 10 min, and 25% O_2.

sccm was near the limit of the MFCs the slightly higher value was used to ensure run to run reproducibility.

To further reduce the degree of Cl_2 exposure we reduced the treatment time from 10 minutes to 0.5 minutes. Figure 3.4 plots the texture coefficient as a function of time. The recrystallization process was observed to occur very quickly. Complete re-crystallization is observed in as short a time as 1 minute under these conditions. Note that the residence time in the reactor is τ~0.5 minutes, so although limited re-

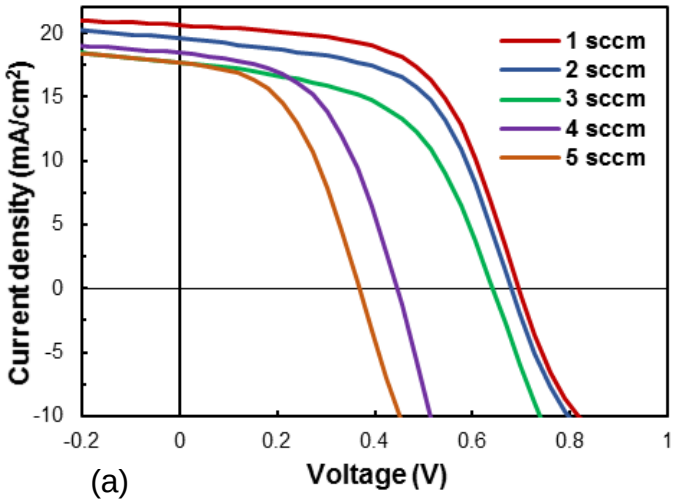

(a)

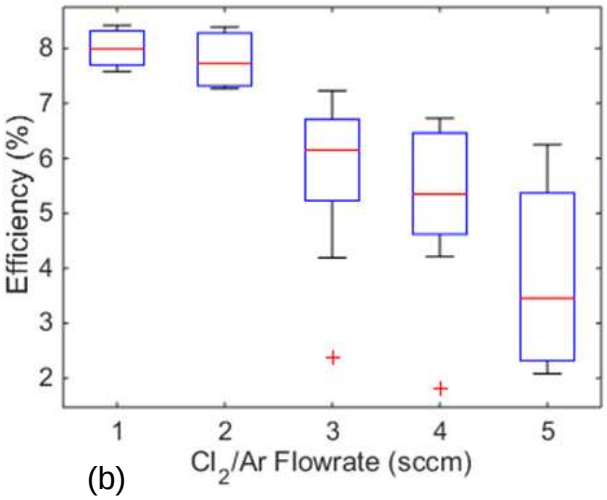

. (b)

Figure 3.3 (a) Representative J-V curves and (b) box plots summarizing device efficiency as a function of Cl_2/Ar flowrate at at T = 400 ºC, t = 10 min, and 25% O_2.

crystallization was observed, the Cl_2 concentration in the reactor was well below steady state levels, as seen in Figure 4. For the remaining runs the exposure time was fixed at t = 2 minutes, the minimum required to establish steady state conditions in the reactor.

A critical parameter is standard $CdCl_2$ activation is the oxygen content in the ambient. Although Komin et al. [51] found that the presence of oxygen during $CdCl_2$ activation had no impact on defect structure, in general it has been reported that O_2 is both necessary and beneficial for optimal device performance [52, 53]. At CSM our standard $CdCl_2$ activation is optimal at 50% O_2, and we obtain poor device performance when no oxygen is present during this step. In stark contrast, it was found with the Cl_2 activation process that the presence of oxygen was detrimental. Figure 3.5 plots the texture coefficient as a function of oxygen content, and from this graph it appears that the presence of oxygen has a negligible impact on the re-crystallization process.

However, as shown in Figure 3.6 the presence of oxygen did affect efficiency. Much like Cl_2 exposure, device efficiency improved as the amount of oxygen was

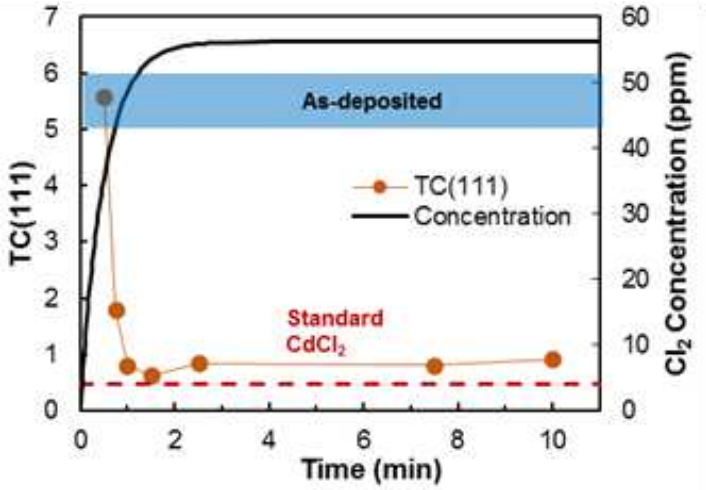

Figure 3.4 (111) texture coefficient as a function of time at T = 400 ºC, t = 2 min, and 1.5 sccm Cl_2/Ar.

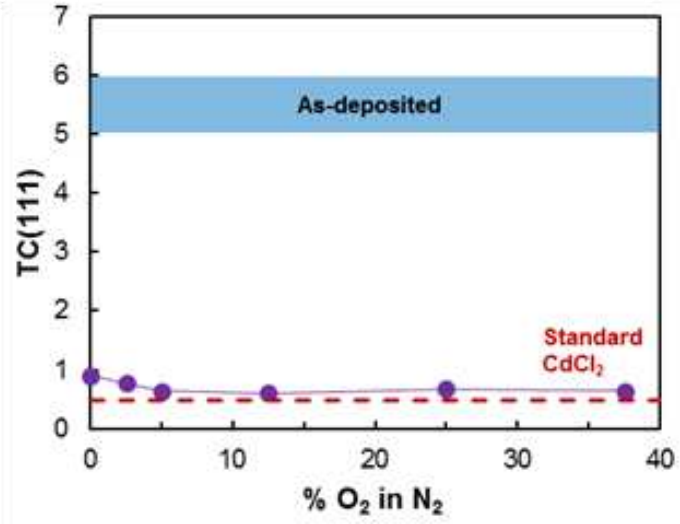

Figure 3.5 TC(111) as a function of oxygen fraction at T = 400 ºC, t = 2 min, and 1.5 sccm Cl_2/Ar.

reduced, with best performance being obtained under pure N_2 flow. As shown in Fig. 3.6a as oxygen is added to the ambient the V_{oc} decreases while the remaining parameters remain largely unchanged until 25%, where there is also a significant decrease in the Jsc value. This suggests that one possible role of O_2 during conventional $CdCl_2$ treatment is

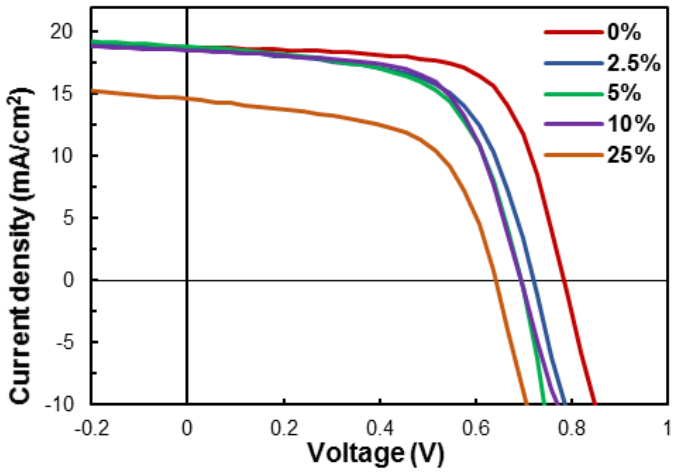

(a)

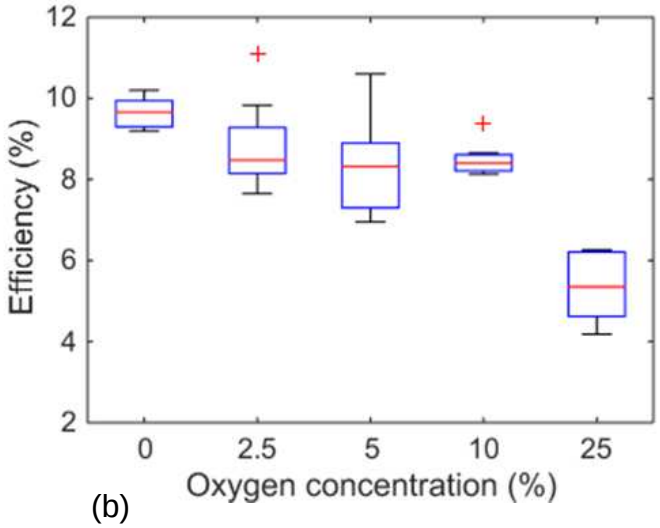

(b)

Figure 3.6 (a) Representative J-V curves and (b) box plots summarizing device efficiency as a function of oxygen content at T = 400 ºC, t = 2 min, and 1.5 sccm Cl_2/Ar.

to oxidize the cadmium that is released upon $CdCl_2$ decomposition, as this is the only chemical difference between the two processes.

To summarize, at this point we have identified that a threshold temperature of T = 400 ºC is required to induce full recrystallization. At this temperature the process is very fast (~1 minute) and the presence of oxygen has no impact on recrystallization. Preliminary device studies showed that best performance was achieved in the absence of oxygen using the minimum degree of Cl_2 exposure that may be reliably delivered in our

current apparatus. In our experience the conventional $CdCl_2$ process is most sensitive to temperature. At 5 ºC below the optimum film performance declines substantially while 5 ºC above often results in delamination of the absorber. As such we revisited the impact of temperature in the absence of oxygen at the lowest reliable Cl_2 exposure (t = 2 minutes, 1.5 sccm).

A significant potential benefit of Cl_2 activation over alternatives like $CdCl_2$ or $MgCl_2$ is latitude with respect to process temperature. With typical treatments the process temperature and exposure are tightly coupled by the vapor pressure. In the case of a gas phase sources such as Cl_2 the degree of exposure and process temperature are completely decoupled, providing new opportunities for process optimization. Figure 3.7 compares the device efficiency obtained by Cl_2 activation as a function of process temperature with devices made under identical conditions using conventional $CdCl_2$ activation at T = 400 ºC.

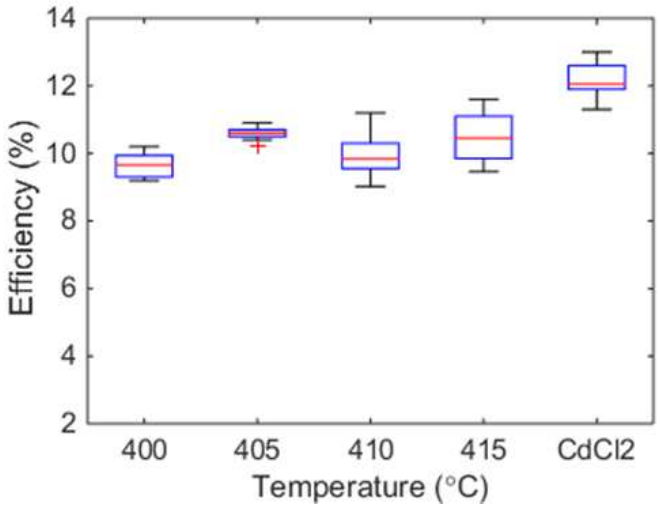

Figure 3.7 Device efficiency as a function of process temperature using 1.5 sccm Cl_2/Ar, 0% O_2, and a treatment time of 2 min.

In the case of Cl_2 activation device efficiency was essentially constant or possibly slightly improved as the temperature was increased from T = 400 to 415 ºC. Note that no delamination was observed over this range of conditions, showing that the Cl_2 activation offers greater process latitude. In addition, under these conditions it was observed that Cl_2 activation provided better uniformity within a sample, better run to run reproducibility, and less deposition than standard $CdCl_2$ activation.

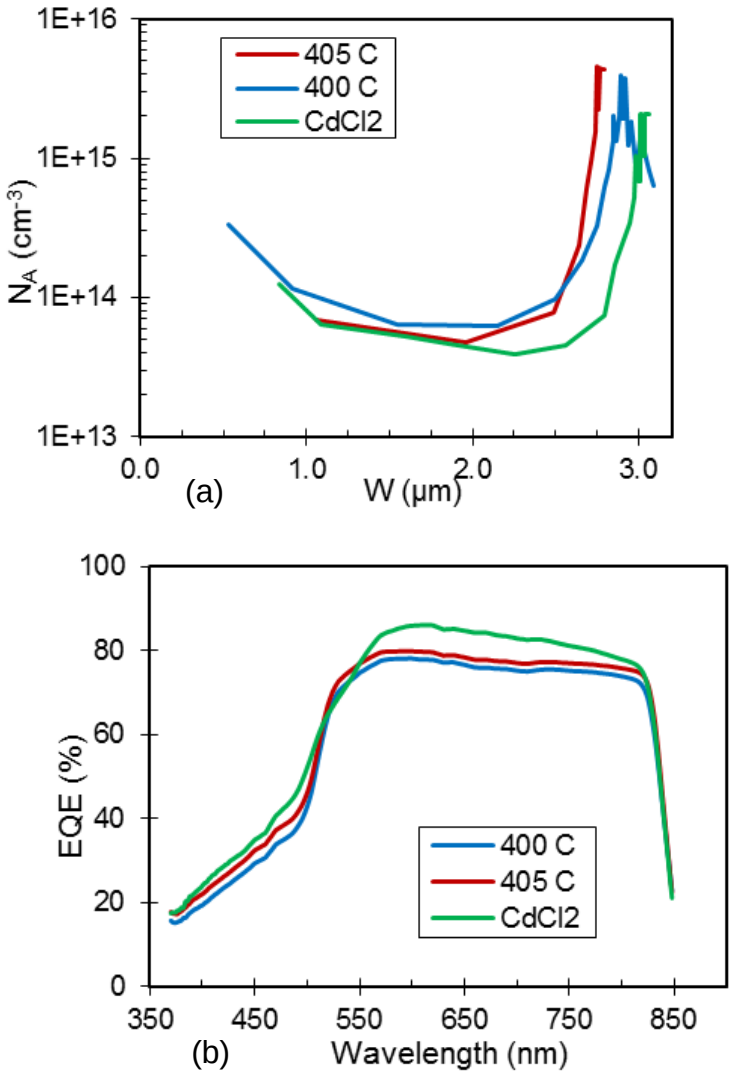

Figure 3.8 Comparison of (a) carrier concentration profiles and (b) EQE curves for Cl_2 activated devices at 400 ºC and 405 ºC with a standard $CdCl_2$ device.

Despite the benefits at this point the efficiency of devices processed with the standard $CdCl_2$ activation exceed those activated by molecular chlorine. To better understand the difference between the two processes we analyzed the resulting devices using capacitance-voltage (CV) profiling and external quantum efficiency (EQE). Figure 3.8a plots the carrier concentration as a function of depletion depth. Both Cl_2 and $CdCl_2$-activated devices display the U-shaped curve characteristic of CdTe solar cells, with similar carrier concentrations on the order of 10^{14} /cm^3. In contrast, significant differences were observed in the EQE spectra (Fig. 3.8b). The response of the Cl_2 devices activated at 400 and 405 ºC were nominally identical, consistent with the JV data. Note that integration of the EQE spectra was in good quantitative agreement with J_{sc} values. The EQE behavior at the band edge was nominally identical. The principle difference observed was in the CdTe collection region between 550- 800 nm, where the EQE of $CdCl_2$ devices was ~10% greater than Cl_2 activated devices. This suggests that at present Cl_2 activation introduces a significant density of defects that increase bulk recombination relative to standard $CdCl_2$ activation. There are also subtle differences in the blue region. In the case of Cl_2 activation the CdS band edge is quite sharp relative to the $CdCl_2$ device. This suggests that the degree of CdS-CdTe interdiffusion was reduced in the former. This is perhaps unsurprising as the duration of Cl_2 activation was just two minutes relative to the 30 minutes used for standard $CdCl_2$. So while process like CdTe recrystallization may be quite fast, other potentially important processes like interdiffusion require additional time.

Finally Figure 3.9 compares the J-V curves of our best Cl_2 activated device (11.6%) with a baseline $CdCl_2$ device (14.5%). An open circuit voltage of 802 mV, a short circuit

current of 21.7 mA cm^{-2}, and a fill factor of 66.4 % was measured for the 11.6 % device.

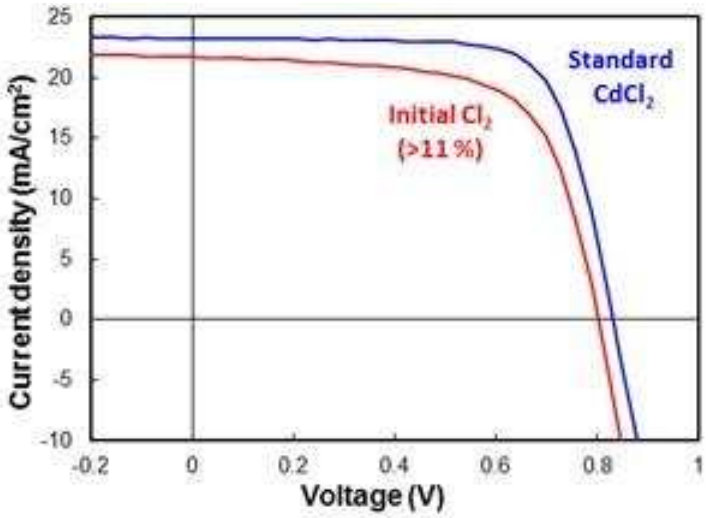

Figure 3.9 Comparison of J-V curves obtained using standard $CdCl_2$ activation and molecular Cl_2 activation.

This is the highest efficiency reported to date for this Cl2 activation, and much higher than several other recently explored alternatives including NH_4Cl, HCl, NaCl, KCl, and $MnCl_2$ [47]. It was processed with 1.5 sccm Cl_2/Ar, T = 415 ºC, 800 sccm N_2, and for 2 min. The results are encouraging as the Cl_2-activated devices display good rectifying behavior and efficiency significantly exceeds previous reports [48]. In addition, we note that under optimal conditions the films are very uniform after Cl2 activation, reflecting the precision and control of gas-phase delivery. Relative to CdCl2 activation device variation is reduced and run to run reproducibility is improved significantly.

3.5 Conclusions

Molecular chlorine was evaluated as an alternative to CdCl2 for post-deposition activation of CdTe solar cells. Several similarities as well as a number of important differences are observed. The process phase space was first screened by using the XRD texture coefficient. It was found that at or above the threshold temperature of 400 ºC, recrystallization occurs very quickly. In stark contrast to conventional $CdCl_2$ it was found that oxygen is detrimental, with best device results obtained using Cl_2/N_2 ambient. Within the parameter space examined it was found that device performance improved as the Cl_2 exposure was reduced. Best device performance was obtained using the minimum Cl_2 exposure that could be reliably delivered in our present system, yielding several devices were fabricated with >11 % efficiency and Voc > 800 mV. It was shown that Cl_2 was equally effective to $CdCl_2$ at generating carriers as their C-V profiles were nominally. The Cl_2-activated devices were somewhat inferior in both current collection and open circuit voltage. EQE analysis revealed that the primary deficiency was excessive recombination within bulk CdTe, suggesting that Cl_2 introduces defects into this region. In addition, it suggests that the degree of CdS-CdTe interdiffusion is somewhat attenuated relative to conventional $CdCl_2$ treated devices. In terms of both uniformity and run to run reproducibility Cl_2 activation was superior, reflecting the improved control provided by the gaseous source. These results indicate that Cl_2 has promise as an alternative to $CdCl_2$. Experiments with further diluted Cl_2 are currently underway to further improve upon these results.

CHAPTER 4

ADDITIONAL AND PRELIMINARY RESULTS

The manuscript reproduced as Ch. 3 contains the most salient and complete results generated over the course of this thesis. This chapter contains additional findings that supplement those findings as well as providing insights that stimulate some of the recommendations for future work discussed in Chapter 5.

4.1 Results from Devices Processed in Excess O_2/Cl_2

As shown in the previous chapter, the best device performance was obtained when Cl_2 activation was performed without oxygen intentionally present. However, as previously mentioned in Chapter 3 the first parameter that was screened with texture coefficient analysis during Cl_2 activation was temperature with all other parameters set to 5 sccm Cl_2/Ar, 10 min, and 25 % O_2. Tracking TC(111) values over the 375 – 415 ºC range indicated that 400 ºC was the threshold temperature for complete recrystallization, thus setting the initial optimal temperature. Devices were fabricated at these conditions and Figure 4.1 presents box plots summarizing the resulting efficiency. In general poor performance was observed (2-5%) and there was no clear trend with respect to substrate temperature. This was somewhat surprising as devices processed below 400ºC had not undergone full recrystallization, but this may be due to the presence of excess Cl_2 and O_2. As shown in Figs. 3.3 and 3.6 device efficiency improved dramatically as these parameters were reduced. However, the results here are consistent with Fig. 3.7 that showed that device efficiency was relatively insensitive to temperature, even under optimized conditions.

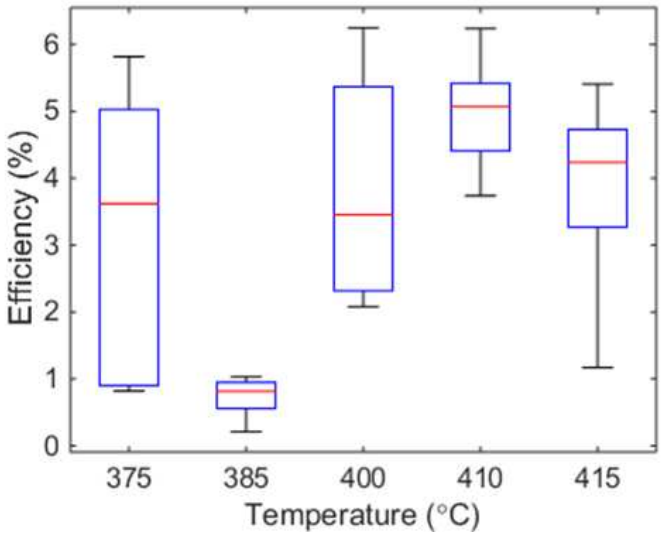

Figure 4.1 Box plots summarizing efficiency results for an initial temperature optimization at t = 10 min, 25% O_2, 5 sccm Cl_2/Ar.

Field emission scanning electron microscope (FE-SEM) images were taken on a JEOL model JSM-7000F in order to further characterize the effects of Cl_2/Ar flow in the presence of oxygen. Images were taken at an accelerating voltage of 10 – 15 kV, ~25,000x, and a working distance of 10 mm. Figure 4.2 displays three representative FE-SEM images. The first (a) shows the as-deposited morphology of CdTe in our standard stack (FTO/CdS/CdTe). This shows the typical polycrystalline morphology with average grain size around 0.5 microns. Figures (b) and (c) shows the morphology after Cl_2 activation using 1 and 5 sccm of Cl_2/Ar, respectively. The remaining parameters were set to 400 ºC, 20% O_2 content, and t = 10 min. Both Cl_2 and $CdCl_2$ activation leave residue on the CdTe which must be removed prior to application of the back contact. This is done by dipping the sample into a 0.05 vol. % Br_2/methanol mixture for 10 s, followed by a methanol rinse. This process smooths the surface and removes the residues.

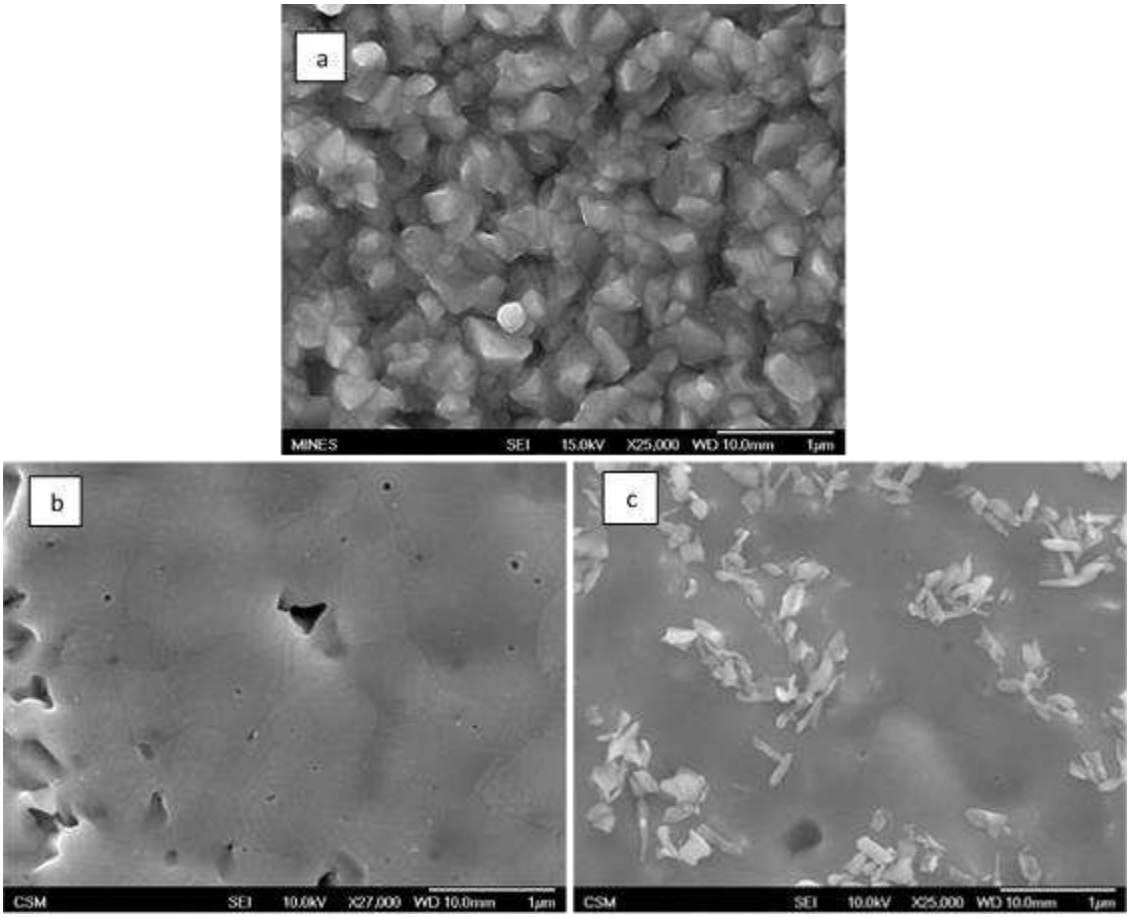

Figure 4.2 Planar FE-SEM images of an CdTe (a) as-deposited and after Cl_2 activation using (b) 1 sccm, and (c) 5 sccm of Cl_2/Ar mixture.

The sample processed using 1 sccm of Cl_2/Ar is very smooth, with no evidence of any remaining precipitates. This is nominally identical to the morphology observed after $CdCl_2$ activation. However as shown in Fig. 4.2c after activation with 5 sccm of Cl_2/Ar the surface is contaminated with a significant precipitates that were not removed by the Br_2/methanol treatment. The precipitates most likely are insulating oxychlorides and are likely a prominent factor in causing the large reduction in device performance at higher Cl_2/Ar flowrates. The precipitates additionally may be a reason why a large oxygen content is detrimental to device performance.

4.2 Attempts to Reduce Cl_2 Exposure

As previously mentioned in Chapter 3, the threshold time for full recrystallization was 1 min, but the optimal time was set to 2 min because the residence time in the reactor is 0.5 min. To support this reasoning, additional devices were fabricated at a shorter exposure time of t = 1 min, 405 ºC, 1.5 sccm Cl_2/Ar, and 800 sccm N_2. Indeed, the devices at the reduced treatment time showed significantly worse performance with a median efficiency of 5.9%. Figure 4.3 compares a top performing device (6.84%) from the 1 min treatment time with a 11% device treated at the same conditions but for 2 min

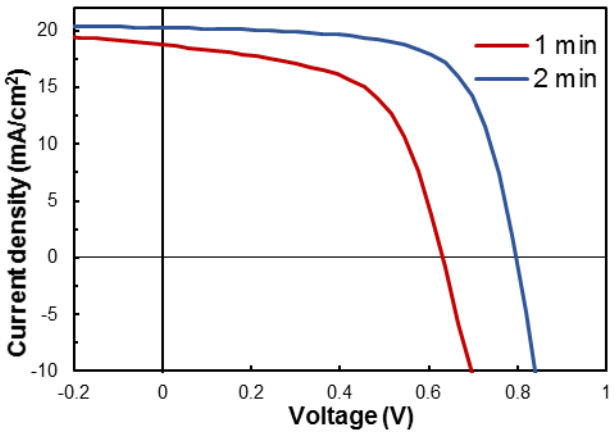

Figure 4.3 Comparison of a 1 min and 2 min activated device.

the open circuit voltage is significantly less for the 1 min treatment, indicating that an under-exposure occurred because steady state conditions could were not obtained.

It is well established that there are three prominent changes induced by $CdCl_2$ activation: (i) recrystallization and grain growth; (ii) Cl passivation of grain boundaries; and (iii) CdS-CdTe interdiffusion at the heterojunction. Another possibility is that 1 minute exposure may have been sufficient to induce recrystallization/passivation, but it may have been insufficient to allow sufficient interdiffusion to occur. Cl_2 exposure is a function of

both concentration and time. It is clear from our study that exposure needs to be reduced, but these results suggest that while the Cl_2 concentration must be reduced, there may be other processes that require additional time.

4.3 TEM Analysis

Courtesy of collaborators in Loughborough University (UK), samples were analyzed using high resolution transmission electron microscopy (HR-TEM) and energy dispersive x-ray (EDX) mapping. The three complete devices that were sent for analysis were (1) an unactivated standard FTO/CdS/CdTe/ZnTe:Cu/Au sample, (2) a sample activated with standard $CdCl_2$, and (3) a sample treated with near optimal Cl_2 activation: T = 415 ºC, 1.5 sccm Cl_2/Ar, 0% O_2, 800 sccm N_2, and t = 2 min. Figure 4.4 compares bright field TEM images of these three devices. The as-deposited film is characterized by a columnar growth morphology. In addition, the grains are defective with a high density of stacking faults. After standard $CdCl_2$ activation the grain size and quality is dramatically improved. The columnar growth morphology is replaced by equiaxed grains that have been formed through coalescence. The stacking faults have disappeared and the only defects that remain are twin boundaries which are common to CdTe. The morphology of the Cl_2-activated device (4.4c) is intermediate to these first two images. There is significant grain growth from the as-deposited state, but the grains are not quite as large and there are areas of lower density (seen as white spots) in the absorber layer. The white spots may indicate the presence of voids due to incomplete grain coalescence. So although XRD shows that the film has fully recrystallized into a random orientation, it will not detect the degree of coalescence seen in these TEM images. The

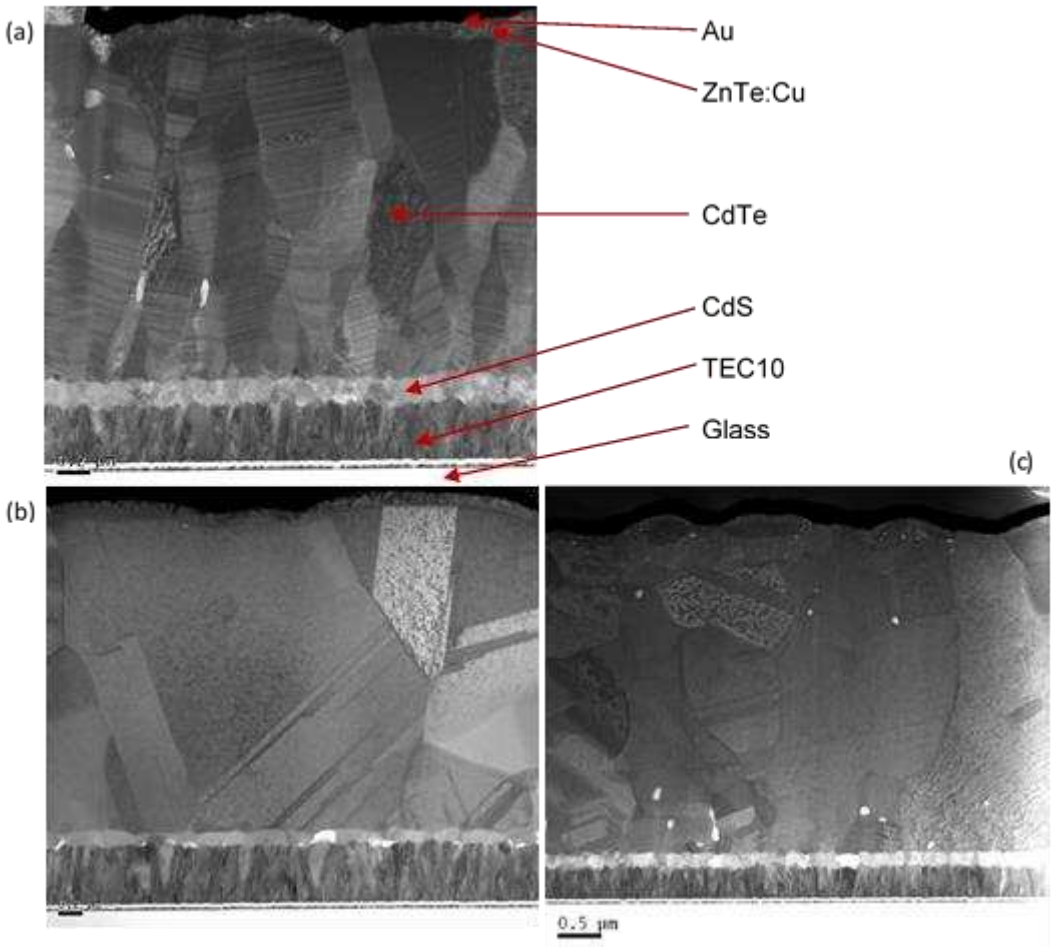

Figure 4.4 BF-TEM images of an (a) un-activated, (b) a $CdCl_2$ treated, and (c) a Cl_2 treated device.

stacking faults are largely removed but the crystal quality remains inferior to the $CdCl_2$ treated device.

Further insight into the difference between $CdCl_2$ and Cl_2 activation were provided by compositional mapping of these sample. Figure 4.5 compares elemental Cl EDX maps from the $CdCl_2$ and Cl_2 activated devices. Note that these maps are qualitative and the limit of detection of EDX is ~ 0.5 at. %. In the case of the $CdCl_2$ treated devices Cl is found to be concentrated in the window layer region of the device. This is consistent with recent XPS profiling has shown that Cl preferentially accumulates

in CdS at levels of ~1 at. % after $CdCl_2$ treatment [24]. Chlorine also decorates the CdTe grain boundaries. In contrast, the Cl map of the Cl_2-activated device shows the presence of substantial Cl accumulation. There is preferential accumulation in CdS and at GBs as expected, but there are also bright clusters of Cl distributed throughout the

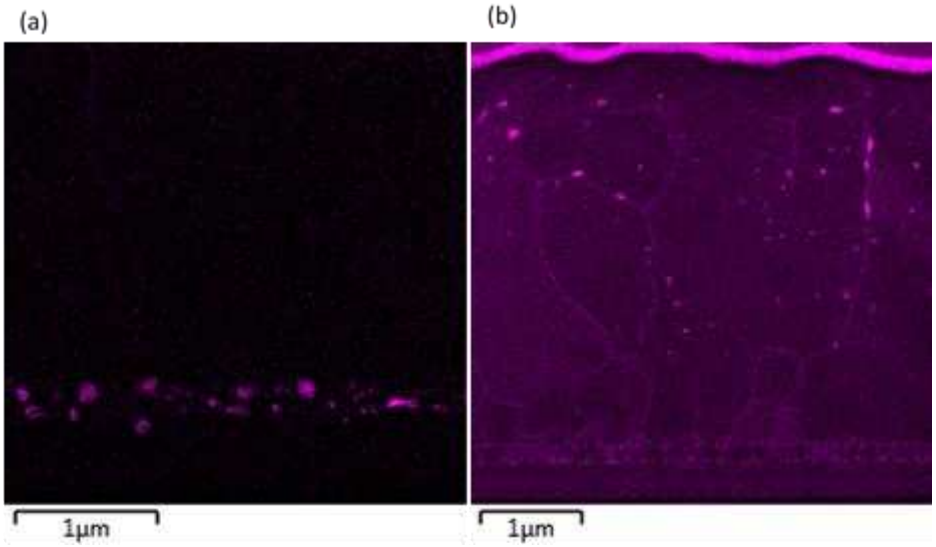

Figure 4.5 Cl EDX maps of (a) a $CdCl_2$ and (b) Cl_2 activated device.

absorber. This is likely a major source for the inferior performance and consistent with our observation that best results were obtained at the lowest Cl_2 densities. The presence of Cl and morphology may be interrelated, in that Cl may be occupying the void space created by imperfect grain coalescence. These images suggest that a combination of lower concentration and perhaps longer exposure times are in order.

A more surprising result was the oxygen distribution as shown in Figure 4.6. No significant oxygen is detected in the absorber of devices activated by standard $CdCl_2$. In contrast there are a number of oxygen-rich clusters present in the Cl_2 activated device. Comparison with the Cl map shows that these clusters are co-located at the exact position of the Cl clusters. The interrelationship between Cl, O, and defects is shown more clearly

in the high resolution elemental mapping images near the back contact of the Cl_2-activated device (Fig. 4.7). Here we clearly see the one to one relationship among Cl impurities, oxygen impurities, and defects which appear as areas of reduced intensity on the Te map. The presence of these defects and impurities certainly explains the inferior.

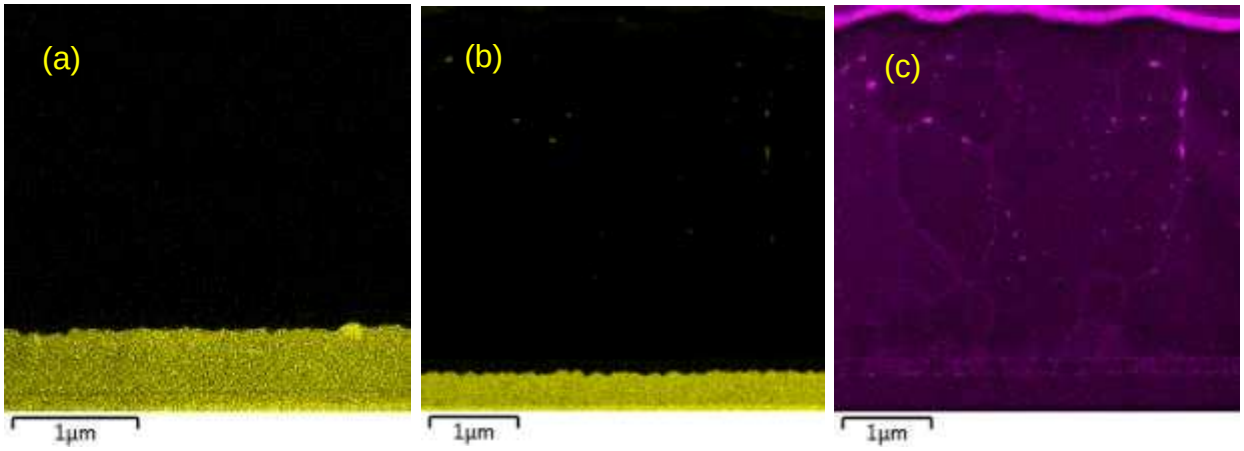

Figure 4.6. O EDX maps for (a) $CdCl_2$ device and (b) Cl_2– activated device. (c) Cl EDX map for comparison.

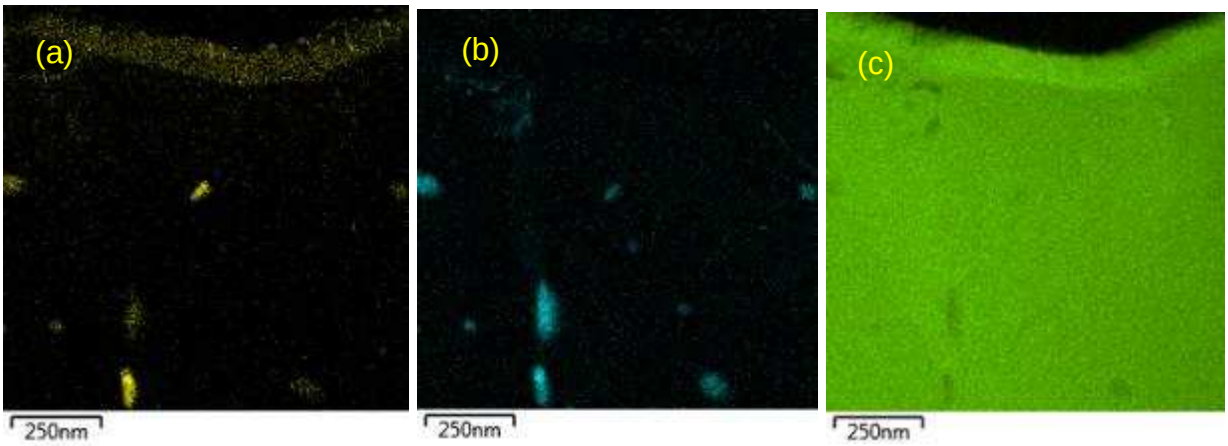

Figure 4.7. High resolution (a) oxygen, (b) chlorine, and (c) tellurium EDX maps from a Cl_2 – activated device near the back contact.

performance of the Cl_2-activated device. In fact it is somewhat surprising that such high efficiency (>11%) was obtained from such poor material. On a positive note it suggests

that performance can be vastly improved upon minimization of such defects/impurities. The presence of oxygen is particularly surprising considering that Cl_2 activation was performed under flowing N_2 and $CdCl_2$ activation occurs in an O_2/N_2 mixture. Potential sources for this are discussed in the next section

4.4 Sources of Unintentional Oxygen

As just discussed the Cl_2-activated devices contain significant levels of oxygen, despite the fact that they were treated under flowing nitrogen. In this section we discuss two possible sources of this oxygen: leaks in the system and contamination due to etching of quartz and/or glass superstrates.

The attachment of a residual gas analyzer (RGA) to the quartz tube furnace identified an oxygen signal in the system that was on the same magnitude as 1 sccm of Ar. After this observation, it was later that discovered that a damaged metal-metal seal was present on a section of the tubing, and after replacing the connection, the oxygen signal was reduced to neglibigle levels. The observation of the oxygen leak with the RGA occurred after all devices reported in the thesis were fabricated. Effects of fabricated devices without the oxygen leak could not be investigated because of temporary closure of the CdTe fabrication lab due to relocation and construction constraints. Future devices should be fabricated without the discovered oxygen leak to determine its effects on device performance.

Another source of oxygen could be the etching of the quartz tube or glass superstrate under the flowing Cl_2/Ar. If the Cl_2 was liberating oxygen from the quartz tube, an alternative material could be used to reduce this effect. Alternative materials are listed in Section 5.2.

Throughout the study it was found that cleaning the quartz tube after each Cl_2 activation was important for experimental reproducibility and may or may not be related to the previously mentioned oxygen contamination. If the tube was not cleaned after each activation, it was found that device efficiencies would reduce by up to 80 % even after only 1 previous treatment. The reduction in efficiency was not as strong when no oxygen was in the ambient during a previous treatment, but after two previous activations without oxygen, the resulting efficiencies were reduced by 80 – 90 %. After an activation treatment the quartz tube was removed from the furnace, fully submerged in deionized water, followed by a nitric acid submersion, and finally rinsed a second bath of deionized water. A cylinder with a cap on end with a 3” diameter was used as a container for the tube bath to allow for easy submersion, and the second deionized water bath never contained water that was exposed to a previous contaminated tube. After the second deionized water bath, the tube was dried under 800 sccm of N_2 at 500 ^oC for 20-40 min before a new sample was activated.

4.5 Investigations of Interdiffusion

As noted in Chapter 3, the EQE spectra suggested that interdiffusion at the heterojunction was reduced using Cl_2 activation relative to standard $CdCl_2$. To further assess this, XRD with liftoff techniques could be used to assess the degree of interdiffusion. A technique was developed to assess the extent of interdiffusion at the junction, but temporary closure of the CdTe lab due to relocation and construction prevented the application of this technique to any Cl_2 activated devices.

Thermo-mechanical liftoff at the FTO|CdS interface allows for characterization of the heterojunction by exposing the CdS side of a CdS/CdTe/ZnTe:Cu/Au stack. The separation occurs by immersion of a completed device in liquid nitrogen and allowing the significant differences in coefficients of thermal expansion of CdS and FTO to cause cleavage at the interface. The procedure consists of applying Loctite 1c epoxy to the back of a completed device, placing an aluminum SEM mount over the epoxy, and letting it cure overnight. After immersion in liquid nitrogen, a cleavage occurs at the interface resulting exposed, mirror-like surfaces.

X-ray diffraction of samples from a post-processed device from the CdS side allows for analysis of the heterojunction region instead of being attenuated by 3-4 µm of CdTe. As a result, high-angle planes will often show doublets that indicate diffraction from bulk CdTe and alloy formation from $CdS_{1-x}Te_x$ [31]. This is a result of recrystallization assisted S diffusion into cubic CdTe. Generally speaking, a hexagonal $CdTe_yS_{1-y}$ alloy is also formed on the CdS side of the junction from Te diffusion, but the primary CdS peak occur at low two theta. By assuming application of Vegard's law to the binary CdTe-CdS alloy system and the cubic lattice constants (a) of CdTe (6.481 Å) and CdS (5.818 Å), the sulfur content (x) can be quantitatively determined in the $CdTe_{1-x}S_x$ film at the heterojunction from its measured lattice constant [31]:

$$a_{CdS_xTe_{1-x}} = x(a_{CdS}) + a_{CdTe}(1-x) \qquad (4.1)$$

Substitution of the cubic CdTe and CdS lattice constants results in the equation becoming: x = 1.508(6.481 – a). A higher resolution scan of the (422) region in a $CdCl_2$

recrystallized sample from the CdS side after liftoff resulted in the following doublet, shown in Figure 4.8. The peak from the alloy is at a higher Bragg angle because S has a smaller atomic radius than Te, giving a smaller d-space. The CdTe and CdS_xTe_{1-x} peaks were deconvoluted using Gaussian fits and Table 4.1 lists the resulting information. Note that the only information needed for the determination of sulfur content (x) in Eq. 4.1 is the lattice constant of the S alloy (6.46 Å).

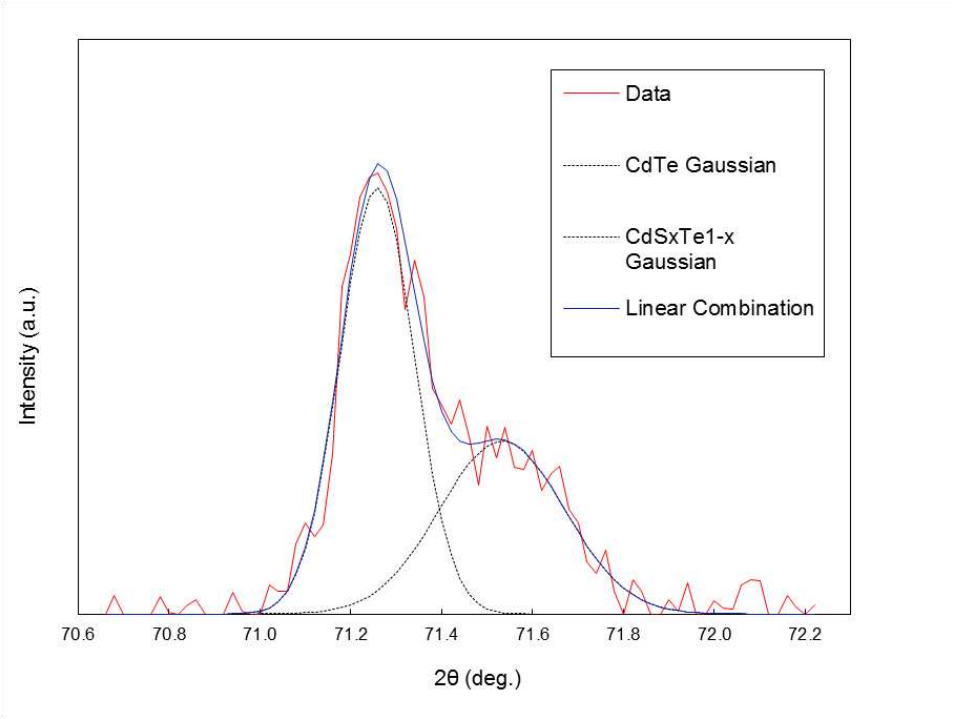

Figure 4.8. Narrow angle scan of the CdTe (422) peak.

Table 4.1. Relevant data from the deconvolution of the CdTe and CdS_xTe_{1-x} (422) peaks.

hkl	2-θ (DEG) CdTe	2-θ (DEG) Sulfur Alloy	d-space Å CdTe	d-space Å S Alloy	lattice constant Å CdTe	lattice constant Å S Alloy	S Content (at. %)
422	71.26	71.53	1.32	1.32	6.48	6.46	3.28

CHAPTER 5

SUMMARY AND CONCLUSIONS

The final chapter consists of a summary of the major findings of the research, followed by a discussion of the important conclusions. Recommendation based on the conclusions are made for future experiments.

5.1 Summary

The activation of thin film CdTe solar cells was performed using molecular Cl_2 as a gas-phase alternative to the conventional $CdCl_2$ treatment. The (111) texture coefficient was used as a figure of merit to identify parameter values of Cl_2/Ar flowrate (1 – 5 sccm), temperature (375 – 420 ºC), oxygen concentration (0 – 25 %), and treatment time (0 – 10 min) that would cause recrystallization of the absorber. Performance was also correlated with TC(111) and process parameters. Cl_2 activation achieved an 11.6 % device, and relative to a standard $CdCl_2$ treatment, reduced treatment time from 30 to 2 min, eliminated the need for O_2, and improved device and run to run variation.

It was found that full recrystallization of the films occurred at the critical temperature of 400 ºC, yielding a TC(111) < 1 that is similar to one obtained from a $CdCl_2$ treated device. For T< 400 ºC, partial recrystallization took place, giving grains that were still preferentially oriented with a TC(111) > 1. The process temperature was set to 400 ºC for future experiments, which is the same temperature for the $CdCl_2$ activation. This indicates that the activation temperature is primarily a function of CdTe and not the source of Cl.

Following temperature, the Cl_2 flowrate was examined by performing experiments with 0.5 – 5 sccm of Cl_2/Ar and T = 400 ºC, t = 10 min, and 25% O_2. Partial recrystallization occurred at 0.5 sccm and with a critical flowrate of ~1 sccm required for TC(111) values similar to a $CdCl_2$ sample. Fabricated devices under these same conditions resulted in an 8 to 3% reduction in efficiency as the flowrate was increased from 1 to 5 sccm, mostly due to V_{oc} dropping from 694 to 368 mV. This trend indicates that over chlorination was occurring, likely due to the enhanced reactivity of Cl_2 over $CdCl_2$. The optimum flowrate was set to 1.5 sccm because 1 sccm was close to the accuracy limits of the MFC.

Although Cl_2 was being injected at minimum flowrates, total exposure was further diminished by reducing time. Full recrystallization occurred very rapidly, in as short as 1 min with TC(111) > 1 at t < 1 min. Because the residence time of the reactor was τ ~0.5 min, the optimum time was set to 2 min to allow for steady state conditions in the reactor during the treatment. This suggests that although recrystallization is necessary for high efficiency, it is not sufficient and other processes are involved.

Experiments with varied oxygen concentration in the ambient at T = 400 ºC, t = 2 min, and 1.5 sccm Cl2/Ar indicated that recrystallization is unaffected by oxygen. J-V measurements indicated that increasing oxygen concentration causes a slight decrease in device efficiency from 0 – 10% O_2 and at 25% O_2 performance significantly compromised. Degradation of device performance is mostly due to loss in V_{oc}, while J_{sc} and FF remain unchanged. This is in constrast to standard $CdCl_2$ activation, where optimization of an oxygen ambient, around 20 - 50%, is required for obtaining quality devices with high V_{oc} and FF.

An additional set of devices were fabricated from T = 400 – 415 ºC at 1.5 sccm, 0% O_2, and t = 2 min. Efficiency was essentially constant throughout this range. This is contrasted with the conventional $CdCl_2$ treatment where a 5 ºC error in temperature setpoint results in delamination and significant loss in performance. Under these optimal conditions, the Cl_2 treatment yielded better uniformity, run to run reproducibility, and less material deposition.

The best performing device was fabricated at 1.5 sccm Cl_2/Ar, T = 415 ºC, 800 sccm N_2 and for 2 min, yielding an open circuit voltage of 802 mV, a short circuit current of 21.7 mA cm^{-2}, a fill factor of 66.4 %, and an 11.6 % efficiency. This 11.6 % efficiency fell short of a standard 14.5 % $CdCl_2$ device. CV profiling indicated that the optimized Cl_2 and standard $CdCl_2$ give similar carrier concentrations at low ~10^{14} cm^{-3} and U-shape profiles. EQE indicates that current is primarily lost by recombination in the absorber with subtle differences in the blue region. FE-SEM planar images show that oxychloride precipitates are found at higher Cl_2/Ar flowrates and in the presence of O_2, which would have contributed to the loss in performance seen in J-V results at higher flowrates. Cross-sectional BF-STEM images show that the Cl_2 treatment results in grain boundary passivation and in the removal of stacking fault defects, similar to $CdCl_2$ treatments. Cl, O, and Te elemental maps from EDX show excessive Cl accumulation and clusters of high O and Cl concentrations are also found that are not seen in the $CdCl_2$ device, where O_2 is intentionally introduced during the activation. Although decent devices fabricated at reduced processing time, improved reproducibility, and lower environmental risk were demonstrated with Cl_2 activation, further improvements in

composition and defect densities need to be obtained from this process in order for performance to become equal to or better than $CdCl_2$ treated devices.

5.2 Recommendations for Future Work

Further research is recommended for the Cl_2 activation because the 3% source gas proved to limit the minimum exposure of Cl_2/Ar to 1.5 sccm and 2 min, and these are the parameters that gave the best performing devices. This is also supported by the significantly greater Cl concentrations found by EDX maps of the device treated at 1.5 sccm and 2 min when compared to a standard $CdCl_2$ device. Purchasing source gas at 0.3 % Cl_2/Ar would allow for smaller flowrates of Cl_2 assuming that the MFC is not changed. Using 1.5 sccm of 3% Cl_2/Ar and 800 sccm of N_2 gives a concentration of 56 ppm Cl_2 and delivering 1-5 sccm of 0.3% Cl_2/Ar in 800 sccm of N_2 allows a sufficient range of concentrations (3.4 – 19 ppm) that is near and below the previous optimization concentration. Additionally, the previous 56 ppm Cl_2 concentration can be obtained from the 0.3 % Cl_2/Ar by delivering 5 sccm of 0.3 % Cl_2/Ar in 267 sccm of N_2.

Results show that an exposure time of < 1 min with 1.5 sccm of 3% Cl_2/Ar results in partial recrystallization and poor device performance. This indicates that longer treatment times with the 0.3% source gas will be needed and will most likely allow for finer optimization of the treatment. Additionally, results indicate that at 10 min and 1 sccm of 3% Cl_2/Ar results in partial recrystallization. Therefore, a maximum treatment time of 20 min should be used to identify if the film can be fully recrystallized with 1-5 sccm of 0.3% Cl_2/Ar. All other parameters should be fixed at 400 ºC, 0% O_2, 800 sccm N_2, and 600 Torr. If 1-5 sccm of 0.3% Cl_2/Ar all result in full recrystallization, the 5

experiments should be repeated at reduced times until a critical flowrate is found that results in partial-recrystallization, as seen in Table 5.1.

Table 5.1. Recommended experiments for a 0.3 % Cl_2/Ar source gas

Experimental Group	0.3 % Cl_2/Ar Flowrate (sccm)	Time (min)	N_2 Flowrate (sccm)	Temperature (℃)
1	1-5	20	800	400
2	1-5	15	800	400
3	1-5	10	800	400

After this time is identified devices should be fabricated at 1-5 sccm, and once an optimal flowrate is identified, the temperature should be varied from 400 – 420 °C.

Interdiffusion studies should also be performed to further understand the effects of Cl_2 activation. The kinetics of interdiffusion can be studied by varying time and temperature, and measuring the S fraction in $CdTe_{1-x}S_x$ by XRD. The conditions for these experiments should use the previously optimized Cl_2/Ar flowrate at times that result in partial to complete recrystallization at each temperature. The extent of interdiffusion should also be compared to a standard $CdCl_2$ device.

Other studies to investigate the effects of an oxygen leak or quartz tube etching should also be carried out as oxygen appeared throughout the CdTe layer even though no oxygen was intentionally delivered. This can be accomplished by monitoring the background oxygen signal with residual gas analyzers and to ensure that processing always occurs without significant O_2 content. Inert tube coatings or alternative tube materials such as stainless steel, graphite, or boron nitride could be used during treatments to determine if the oxygen is due to reaction of the tube surface with Cl_2.

REFERENCES CITED

1) Key World Energy Statistics 2015. International Energy Agency. OECD/IEA. Web. 22 Feb. 2016, from https://www.iea.org/publications/freepublications/publication/key-world-energy-statistics-2015.html

2) U.S. Energy Information Administration. EIA. Independent Statistics and Analysis. (n.d.). Web. 25 Feb. 2016, from http://www.eia.gov/consumption

3) M. Leduc, H. D. Matthew, and R. D. Elía, “Regional estimates of the transient climate response to cumulative CO_2 emissions,” Nature Climate Change Nature Climate change, vol. 6, pp. 474-478

4) K. Zweibel, “The terawatt challenge for thin-film PV,” NREL, Technical Report NREL/TP-520-38350, August, 2005

5) N. Lewis, “Powering the Planet,” Caltech, The Lewis Group, http://www.its.caltech.edu/~mmrc/nsl/energy.html .

6) 2014 Renewable Energy Data Book. US Department of Energy. http://www.nrel.gov/docs/fy16osti/64720.pdf

7) Electric Power Monthly. EIA. Web. 1 March 2016, from https://www.eia.gov/electricity/monthly/epm_table_grapher.cfm?t=epmt_5_3

8) M. Bolinger, J. Seel, “Utility-scale solar 2014,” Berkeley Lab, US Department of Energy, Web., from https://emp.lbl.gov/sites/all/files/lbnl-1000917_presentation.pdf

9) D. Neamen, “Semiconductor physics and devices: basic principles,” McGraw-Hill. 2003

10) PN Junction Theory for Semiconductor Diodes. Basic Electronics Tutorials. 2013. Web. 3 Mar. 2016, from http://www.electronics-tutorials.ws/diode/diode_2.html

11) Types of Recombination. Photovoltaic Education Network. 1 Mar. 2016, from http://www.pveducation.org/pvcdrom/pn-junction/types-of-recombination

12) K. Durose, How PV works, University of Liverpool, Solar Photovoltaics Research group, from

https://www.liverpool.ac.uk/renewable-energy/people-stephenson-institute-for-renewable-energy/ken-durose/

13) A. Luque, S. Hegedus, Handbook Of Photovoltaic Science and Engineering; Wiley: Hoboken, NJ, 2003. Chapter 3. The Physics of the Solar Cell.

14) S. G. Kumar, K. S. R. K. Rao, “Physics and chemistry of CdTe/CdS thin film heterojunction photovoltaic devices: fundamental and critical aspects,” Energy & Environmental Science, vol. 7, pp. 45–102, 2014

15) P. Sinha, M. de Wild-Scholten, A. Wade, and C. Breyer, “Total cost of electricity pricing of photovoltaics,” presented at EU PVSEC 2013.

16) Z. Banyamin, P. Kelly, G. West, and J. Boardman, “Electrical and optical properties of fluorine doped tin oxide thin films prepared by magnetron Sputtering,” Coatings, vol. 4, pp. 732-746, 2014

17) J. Jordan and S. Albright, U.S. Patent 5,279,678 (1994)

18) X. Wu, “High-efficiency polycrystalline CdTe thin-film solar cells,” Solar Energy, vol. 77, pp 803-814, 2004

19) T. A. Nguyen, Dissertation, University of Cincinnati

20) H. Metin, R. Esen, “Annealing effects on optical and crystallographic properties of CBD grown CdS films,” Semiconductor Science and Technology, vol. 18, pp. 647-654, 2003

21) T.L. Chu, S.S. Chu, N. Schultz, C. Wang, and C.Q. Wu, “Solution-grown CdS films for photovoltaic devices,” Journal of Electrochemical Society, vol. 139, pp. 2443-2446,1992

22) Y. Lee, W. Lee, Y. Kwon, G. Yeom, and J. Yoon, “Effects of CdS substrates on the physical properties of polycrystalline CdTe films,” Thin Solid Films, vol. 341, pp. 172-175, 1999

23) H. Uda, H. Yonezawa, Y. Ohtsubo, M. Kosaka, and H. Sonomura, “Thin CdS films prepared by metalorganic chemical vapor deposition,” Solar Energy Materials and Solar Cells, vol. 75, pp. 219-226, 2003

24) N.Romeo, A. Bosio, R. Tedeschi, A. Romeo, V. Canevari, and D. Leone. In Proceedings of 14th European Photovoltaic Solar Energy Conference, Barcelona, Spain, pages 2351–2352, 1997

25) B. McCandless, I. Youm, and R. Birkmire, “Optimization of vapor post-deposition processing for evaporated CdS/CdTe solar cells,” Progress in Photovoltaics, vol. 7, pp. 21–30, 1999

26) T.L. Chu, S.S. Chu, C. Ferecides, C.Q. Wu, J. Britt, and C. Wang, “13.4% efficient thin-film CdS/CdTe solar cells,” Journal of Applied Physics, vol. 70, pp. 7608, 1991

27) R. Powell, U.S. Patent 5,945,163, 1999

28) R. Wendt, A. Fischer, D. Grecu, and A. Compaan A, “Improvement of CdTe solar cell performance with discharge control during film deposition by magnetron sputtering, “ Journal of Applied Physics, vol. 84, pp. 2920–2925, 1998

29) G. Fulop, M. Doty, P. Meyers, J. Betz, and C.H. Liu, “High-efficiency electrodeposited cadmium telluride solar cells,” Applied Physics Letters, vol. 40, pp. 327, 1982

30) I. M. Dharmadasa, O. K. Echendu, F. Fauzi, N. A. AbdulManaf, H. I. Salim, T. Druffel, R. Dharmadasa and B. Lavery, “Effects of CdCl2 treatment on deep levels in CdTe and their implications on thin film solar cells; a comprehensive photoluminescence study,” Journal of Materials Science: Materials in Electronics, vol. 26, pp. 4571-4583, 2015

31) B. E. McCandless, L. V. Moulton, and R. W. Birkmire, "Recrystallization and sulfur diffusion in CdCl2-treated CdTe/CdS thin films," Prog in Photovoltaics: Research and Applications, vol. 5, pp. 249-260, 1997

32) H. R. Moutinho, M. M. Al-Jassim, D. H. Levi, P. C. Dippo, and L. L. Kazmerski, "Effects of CdCl2 treatment on the recrystallization and electro-optical properties of CdTe thin films," Journal of Vacuum Science & Technology A, vol. 16, pp. 1251-1257, 1998

33) S. P. Harvey, G. Teeter, H. Moutinho, and M. M. Al-Jassim, "Direct evidence of enhanced chlorine segregation at grain boundaries in polycrystalline CdTe thin films via three-dimensional TOF-SIMS imaging," Progress in Photovoltaics: Research and Applications, vol. 23, pp. 838-846, 2015.

34) T. Paulauskas, C. Buurma, E. Colegrove, Z. Guo, S. Sivananthan, and M. K. Y. Chan, "Atomic-resolution characterization of the effects of CdCl2 treatment on poly-crystalline CdTe thin films," Applied Physics Letters, vol. 105, 2014

35) I. V. Fisher, K. D. Dobson, J. Nair, E. Bezalel, G. Hodes and D. Cahen, "Factors affecting the stability of CdTe/CdS solar cells deduced from stress tests at elevated temperature," Advanced Functional Material, vol. 13, pp. 289-299, 2003

36) C. Ferekides, J. Britt, "Thin film CdS/CdTe solar cell with 15.8% efficiency," Applied Physics Letters, vol. 62, pp. 2851–2852, 1993

37) J. Li, D. R. Diercks, T. R. Ohno, C. W. Warren, M. C. Lonergan, J. D. Beach, et al., "Controlled activation of ZnTe:Cu contacted CdTe solar cells using rapid thermal processing," Solar Energy Mater. Solar Cells, vol. 133, pp. 208-215, 2015

38) T.A. Gessert, "Development of rf sputtered, Cu-doped ZnTe for use as a contact interface layer to p-CdTe," Journal of Electronic Materials, vol. 24, pp. 1443-1449, 1995

39) R. W. Birkmire, B. E. McCandless and S. S. Hegedus, "Effects of processing on CdTe/CdS materials and devices", International Journal of Solar Energy, vol. 12, pp. 145-154, 1992

40) V. Valdna, F. Buschmann and E. Mellikov, "Conductivity conversion in CdTe layers", Journal of Crystal Growth, vol. 161, pp. 164–167, 1996

41) S. A. Ringel, A. W. Smith, M. H. MacDougal ,and A. Rohatgi, "The effects of CdCl2 on the electronic properties of molecular-beam epitaxially grown CdTe/CdS heterojunction solar cells", Journal of Applied Physics, vol. 70, pp. 881–889, 1991

42) L. Vaillant, N. Armani, L. Nasi, G. Salviati, A. Bosio, S. Mazzamuto and N. Romeo, "Interface properties of HCF2Cl annealed CdTe thin films for solar cells applications," Thin Solid Films, vol. 516, pp. 7075–7078, 2008

43) A. Rios-Flores, O. Arés, J. M. Camacho, V. Rejon, and J. L. Peña, "Procedure to obtain higher than 14% efficient thin film CdS/CdTe solar cells activated with HCF2Cl gas," Solar Energy, vol. 86, pp. 780-785, 2012.

44) A. Salavei, I. Rimmaudo, F. Piccinelli, P. Zabierowski, and A. Romeo, "Study of difluorochloromethane activation treatment on low substrate temperature

deposited CdTe solar cells," Solar Energy Materials and Solar Cells, vol. 112, pp. 190-195, 2013

45) Y. Qu, P. V. Meyers, and B. E. McCandless, "HCl vapor post-deposition heat treatment of CdTe/CdS films," in Photovoltaic Specialists Conference, Conference Record of the Twenty Fifth IEEE, 1996, pp. 1013-1016

46) J. D. Major, R. E. Treharne, L. J. Phillips, and K. Durose, "A low-cost non-toxic post-growth activation step for CdTe solar cells," Nature, vol. 511 pp. 334–337 2014

47) B. L. Williams, J. D. Major, L. Bowen, W. Keuning, M. Creatore, and K. Durose, "A Comparative Study of the Effects of Nontoxic Chloride Treatments on CdTe Solar Cell Microstructure and Stoichiometry," Advanced Energy Materials, pp. 543, 2015

48) T. X. Zhou, N. Reiter, R. C. Powell, R. Sasala, and P. V. Meyers, "Vapor chloride treatment of polycrystalline CdTe/CdS films," in First World Conference on Photovoltaic Energy Conversion, 1994, pp. 103-106

49) P. V. Meyers, C. H. Liu, and T. J. Frey, "Method of making photovoltaic cell with chloride dip," US Patent, 1989.

50) D. Bonnet, "Manufacturing of CSS CdTe solar cells," Thin Solid Films, vol. 361–362, pp. 547-552, 2000

51) V. Komin, B. Tetali, V. Viswanathan, S. Yu, D. L. Morel, and C. S. Ferekides, "The effect of the CdCl2 treatment on CdTe/CdS thin film solar cells studied using deep level transient spectroscopy," Thin Solid Films, vol. 431–432, pp. 143-147, 2003

52) D. S. Albin, S. H. Demtsu, and T. J. McMahon, "Film thickness and chemical processing effects on the stability of cadmium telluride solar cells," Thin Solid Films, vol. 515, pp. 2659, 2006

53) E. Regalado-Perez, M. G. Reyes-Banda, and X. Mathew, "Influence of oxygen concentration in the CdCl2 treatment process on the photovoltaic properties of CdTe/CdS solar cells," Thin Solid Films, vol. 582, pp. 134-138, 2015